

OPEN ACCESS

Interaction of Pore Size and Hydrophobicity/Hydrophilicity for Improved Oxygen and Water Transport through Microporous Layers

To cite this article: Christoph Simon *et al* 2019 *J. Electrochem. Soc.* **166** F1022

View the [article online](#) for updates and enhancements.



Interaction of Pore Size and Hydrophobicity/Hydrophilicity for Improved Oxygen and Water Transport through Microporous Layers

Christoph Simon,^{1,*} Joseph Endres,¹ Benjamin Nefzger-Loders,¹ Florian Wilhelm,² and Hubert A. Gasteiger^{1,**}

¹Chair of Technical Electrochemistry, Department of Chemistry and Catalysis Research Center, Technical University of Munich, D-85748 Garching, Germany

²Centre for Solar Energy and Hydrogen Research Baden-Wuerttemberg, Division 3, Electrochemical Energy Storage and Conversion, D-89081 Ulm, Germany

Microporous layers consisting of different ratios of acetylene black and carbon fibers with either a hydrophobic polytetrafluoroethylene (PTFE) or a hydrophilic perfluorosulfonic acid (PFSA) ionomer binder are investigated with regards to oxygen and water transport in PEMFCs. For that, the materials are characterized by scanning electron microscopy and mercury porosimetry, revealing an increase of porosity and pore sizes for an increasing carbon fiber content. MPLs, coated onto a commercial hydrophobized non-woven gas diffusion layer substrate, are examined in H₂/air fuel cell tests under differential-flow conditions at various dry and humid operating conditions. For both hydrophobic and hydrophilic MPLs in the presence of significant amounts of liquid water in the diffusion layer substrate, the materials with larger pore sizes, i.e. higher carbon fiber contents, perform superior at 0.6 V and show the lowest oxygen transport resistance. However, at the same carbon composition, hydrophilic MPLs have a lower performance compared to the corresponding hydrophobic MPLs, which is explained by the capillary pressure barriers for different pore properties. At operating conditions relevant for automotive applications, a performance enhancement of 48% could be achieved for a purely carbon fiber based MPL compared to a commercial reference.

© The Author(s) 2019. Published by ECS. This is an open access article distributed under the terms of the Creative Commons Attribution Non-Commercial No Derivatives 4.0 License (CC BY-NC-ND, <http://creativecommons.org/licenses/by-nc-nd/4.0/>), which permits non-commercial reuse, distribution, and reproduction in any medium, provided the original work is not changed in any way and is properly cited. For permission for commercial reuse, please email: oa@electrochem.org. [DOI: 10.1149/2.1111913jes]



Manuscript submitted June 17, 2019; revised manuscript received August 12, 2019. Published September 10, 2019.

Polymer electrolyte membrane fuel cells (PEMFC) require efficient transport pathways for reactant gases (O₂ and H₂) and product water in order to reach high current densities. The depletion of oxygen at the cathode electrode is one of the major sources of overpotentials at high current densities, which is particularly relevant at conditions of high liquid water saturation in the cell.^{1–3} The gas diffusion layer (GDL) is the intermediate layer between the gas flow fields and the electrode layers, and is responsible for species transport (O₂/H₂, H₂O), heat removal, and compression distribution. It consists of a carbon fiber-based gas diffusion layer substrate (GDL-S), which is conventionally coated with a microporous layer (MPL). Both the GDL-substrate and the MPL are typically hydrophobically treated with PTFE in order to prevent the flooding of the pores.^{4–7}

With its smooth surface, the MPL creates a close contact to the electrode layers, which reduces contact resistances and mitigates the accumulation of liquid water at the interface between GDL-S/MPL and the electrode layer. The MPL is ≈20–50 μm in thickness and has pore sizes on the order of 100–500 nm, much smaller than that of the substrate of ≈10–30 μm.^{4,8} It thus represents a layer with a network of small pores, which moves liquid water accumulations away from the electrode toward the GDL-substrate, because small hydrophobic pores are unlikely to store liquid water. Thus, implementing an MPL reduces the overall water fraction in the porous layers, which in turn allows fast oxygen diffusion from the GDL-substrate toward the cathode even at conditions of liquid water condensation.^{3,9,10}

The MPL typically consists of one or more carbon materials (carbon black, graphite, etc.) and 10–30 wt% of polymer binder (e.g. PTFE) which stabilizes the layer and serves as hydrophobic agent.^{4,11–13} Depending on the choice and composition of materials as well as the manufacturing procedure, different properties of the microporous layer can be adjusted, such as porosity/pore size distribution,^{13–20} hydrophobicity/hydrophilicity,^{21–31} and surface morphology.^{6,32} These parameters influence the oxygen and water transport through the layer, and hence, also the overall fuel cell performance. Porosity and pore

interconnection which can be influenced by the type of carbon, by a combination of different carbon materials, and/or by additional perforations determine the effective diffusivity of gas through the layer. Particularly at humid conditions, cracks, regular perforations, and large pores serve as effective water transport pathways and were shown to prevent flooding of the layers and interfaces.^{15,33,34} Additionally, Tanuma et al. have shown for hydrophilic MPLs that the fuel cell performance is enhanced for carbon materials that result in high porosities.^{19,35} Further studies have shown that the hydrophilicity in MPLs can enhance fuel cell performance due to a hypothesized storage of water in hydrophilic pores, which are thought to (i) keep electrodes and membrane hydrated under low relative humidity conditions, and to (ii) facilitate liquid water release from the electrode through the microporous layer by a wicking effect. Thus, the best-performing hydrophilic MPLs prepared by Tanuma and co-workers were based on ionomer binder and carbon fibers.^{23,24,30} Another example are the various MPLs prepared by Kitahara et al., based on either (i) carbon black with TiO₂/silicon binder or with PVA binder coated on a hydrophobic sublayer MPL, or (ii) on hydrophilic carbon nanotubes with PTFE binder.^{25–27,36,37} Furthermore, a study by Spornjak et al. showed improved oxygen transport and better fuel cell performance for MPLs containing hydrophilic multiwalled carbon nanotubes (MWCNT) or hydrophilic aluminosilicate fibers when compared to a commercial hydrophobic MPL; the authors ascribed the superior performance of the fiber based MPLs to the creation of hydrophilic and hydrophobic domains in the MPL.³¹ A different paper by Lee et al. using the same MWCNT material is showing similar results, however attributing the improvements in water transport rather to the larger pore sizes present in the MPL with MPLs the multiwalled carbon nanotube containing MPL.³⁸ On the other hand, Shrestha and et al. reported an increased water saturation at the electrode/MPL interface and a higher mass transport resistance of a GDL with an MPL consisting of a hydrophilic top-layer placed onto a hydrophobic sublayer.³⁹ However, recently Aoyama et al.³⁰ reported an analysis of both hydrophilic and hydrophobic MPLs with identical structural properties with respect to porosity, pore size distribution (PSD), and thickness, evaluating the differential-flow H₂/air performance of these MPLs. As will be discussed later, some of their findings are at variance with our H₂/air

*Electrochemical Society Member.

**Electrochemical Society Fellow.

²E-mail: christoph.simon@mail.de

performance data and are also inconsistent with our oxygen transport resistance data, which had not been provided in their study.

An important parameter to describe the behavior of liquid water within a microporous structure is the capillary pressure (p_c) determined by the Young-Laplace equation:

$$p_c = p_l - p_v = \frac{4 \cdot \gamma_{\text{H}_2\text{O}} \cdot \cos \theta}{d_{\text{pore}}} \quad [1]$$

where p_l is the liquid phase pressure, p_v is the vapor phase pressure, $\gamma_{\text{H}_2\text{O}}$ is the surface tension of water, θ is the inner contact angle of water with the pore surface, and d_{pore} is the pore diameter. This pressure has to be overcome for water in order to penetrate into a hydrophobic pore ($90^\circ < \theta < 180^\circ$, for which $p_c < 0$ kPa) or to deplete a water filled hydrophilic pore ($0^\circ < \theta < 90^\circ$, for which $p_c > 0$ kPa). Both θ and d_{pore} determine the magnitude of p_c , hence, by modifying either one or both one can tune the liquid water transport properties of the material.^{40,41}

To analyze the oxygen transport properties of gas diffusion layers in PEM fuel cells, the measurement of the limiting current density (i_{lim}) under differential-flow conditions is a valuable method.^{15,33,42–48} Knowing the dry oxygen content in the feed gas ($x_{\text{O}_2,\text{dry}}$), the cell temperature (T_{cell}), the absolute gas pressure (p_{abs}), and the partial pressure of water vapor ($p_{\text{H}_2\text{O}}$), the oxygen transport resistance ($R_{\text{T,O}_2}$) of the cell can be calculated:

$$R_{\text{T,O}_2} = \frac{4 \cdot F \cdot x_{\text{O}_2,\text{dry}}}{i_{\text{lim}}} \cdot \frac{p_{\text{abs}} - p_{\text{H}_2\text{O}}}{R \cdot T_{\text{cell}}} \quad [2]$$

Here, $R_{\text{T,O}_2}$ is composed of the sequential diffusion resistances of oxygen transport from the flow field channels to the active sites of the catalyst layer:

$$R_{\text{T,O}_2} = R_{\text{FF,O}_2} + R_{\text{GDL-S,O}_2} + R_{\text{MPL,O}_2} + R_{\text{cathode,O}_2} + R_{\text{other,O}_2} \quad [3]$$

where $R_{\text{FF,O}_2}$ is the resistance within the flow field channels, $R_{\text{GDL-S,O}_2}$ is the resistance of the GDL-substrate, $R_{\text{MPL,O}_2}$ is resistance of the MPL, $R_{\text{cathode,O}_2}$ is the resistance of the cathode catalyst layer, and $R_{\text{other,O}_2}$ is the remaining resistance from other sources (e.g., interfacial resistances between catalyst layer and MPL⁴⁷). The resistances can be discerned into pressure dependent ($R_{\text{PD,O}_2}$) and pressure independent ($R_{\text{PI,O}_2}$) contributions, the former being associated with molecular diffusion processes mostly in the gas diffusion layer and MPL, while the latter is ascribed to Knudsen diffusion in the small pores of the cathode catalyst layer and to diffusion to the platinum catalyst surface across a thin ionomer film so that it increases with decreasing platinum surface area.^{43,49,50}

In our previous studies, we have already applied the limiting current density diagnostic to determine interfacial transport resistances originating from the formation of liquid water films as a function of diffusion medium compression as well as to examine the impact of different carbon blacks and MPL perforations on the oxygen transport resistance of microporous layers.^{15,47,51} The first scope of the present study is to examine the impact of MPL porosity and pore size distribution (PSD) on the oxygen and water transport in an operating fuel cell. For this, we first prepare microporous layers with polytetrafluoroethylene (PTFE) as hydrophobic binder and different mixtures of carbon black and carbon fibers (between 0 and 100wt%), and then characterize them with scanning electron microscopy and mercury intrusion porosimetry. These MPLs are coated onto commercial GDL-substrate (Freudenberg) and tested in a differentially operated single-cell fuel cell under dry and humid conditions in order to correlate the morphological properties of MPLs with differential-flow H₂/air performance, with the associated high frequency resistances, and with oxygen transport resistances quantified by limiting current density measurements. The second scope of this study is to determine the differences in performance and oxygen transport resistance caused by replacing the hydrophobic with a hydrophilic binder, while maintaining the same MPL morphology (i.e., same carbon composition, thickness, porosity, and pore size distribution). For this, we prepare two MPLs with hydrophilic perfluorosulfonic acid (PFSA) ionomer as binder and compare their oxygen transport resistances and their H₂/air performances to those obtained with hydrophobic MPLs with the same carbon composition

and MPL morphology. With this study, we show how oxygen and water transport are impacted by the MPL porosity/PSD and rigorously prove that all-hydrophilic MPLs are actually decreasing performance in the presence of liquid water.

Experimental

MPL and GDL-Substrate materials.—The acetylene black Li400 (Denka; specifications: spec. surface area = 39 m² g⁻¹, average particle size = 48 nm) and the vapor grown carbon fibers VGCF-H (Showa Denko; specifications: spec. surface area = 13 m² g⁻¹, fiber length = 10–20 μm, fiber diameter = 150 nm) are used as carbon components for the MPLs. Two different binders were used: (i) a hydrophobic PTFE agent and binder (58wt% PTFE dispersion TF 5035GZ from 3M Dyneon) with an average particle size of 200 nm; (ii) a hydrophilic PFSA agent and binder, namely a low equivalent weight PFSA ionomer in a water/alcohol dispersion with an ionomer content of 20wt% (700 EW from Asahi Kasei). As solvent for the MPL ink, either deionized water (Milli-Q, 18 MΩ cm) or 1-propanol (SigmaAldrich) is used. To tune the dispersibility and rheological properties of the PTFE containing inks, Triton X-100 (Sigma Aldrich) and methyl cellulose (SigmaAldrich) are admixed. The compositions of the inks used for the preparation of all the MPLs in this study as well as the final MPL compositions are given in Table I.

As a reference GDL-S/MPL material, a commercially available GDL-substrate with a commercial MPL (Freudenberg) is used, which consists of a ≈50 μm thick MPL composed of carbon black and a hydrophobic binder, applied onto a GDL-S (Freudenberg; hydrophobically treated, ≈154 ± 10 μm thick). The same GDL-substrate was used for the preparation of MPL coatings in the present study, so that when comparing different cathode GDL-S/MPL variants, the only difference is the MPL. The commercially available GDL-S/MPL and GDL-S examined here are the same as those which we had used in our previous study.¹⁵

Preparation of hydrophobic MPLs.—MPLs with PTFE as binder are prepared as described in our previous work¹⁵ for the pure carbon black MPLs. The here called “0% VGCF MPL” is the same as the one referred to as “Li400 MPL” in Reference 15. While for the pure carbon black or pure VGCF MPLs only one carbon component is used (0% or 100% VGCF MPL), for MPLs with 50% and 80% VGCF, the respective amounts of carbon black and carbon fibers are added. Table I lists all ink compositions; it also lists the final MPL compositions after an initial drying on air at 80°C and a subsequent thermal treatment under air with a final temperature of 380°C to decompose Triton X-100 and the methyl cellulose as well as to evenly spread out the PTFE particles. Free-standing MPLs used for MPL mercury porosimetry analysis were prepared by coating the MPL inks onto a smooth glass plate instead of the GDL-substrate, followed by drying at 80°C and removal from the glass plate by a razor blade. For more details, see Reference 15.

The final thickness of the MPL coated onto the GDL-S (d_{MPL}) is determined with a dial gauge (Mitutoyo series 543; ±3 μm accuracy) by taking the thickness of the GDL-S/MPL at five positions ($d_{\text{GDL-S+MPL}}$) and subtracting the thickness of the GDL-S ($d_{\text{GDL-S}}$) that is measured at 8 positions around the coated area:

$$d_{\text{MPL}} = d_{\text{GDL-S+MPL}} - d_{\text{GDL-S}} \quad [4]$$

Based on these measurements, all MPLs considered for fuel cell testing in this study have an MPL thickness of $d_{\text{MPL}} = 30 \pm 5$ μm.

Preparation of hydrophilic MPLs.—MPLs with PFSA ionomer as hydrophilic agent and binder are prepared as follows. Carbon components and 1-propanol (see Table I) are combined in a 100 ml polypropylene cup which is fixed into a cooling holder maintained at ≈0°C (Thinky 250AD-COOL). The substances are mixed for 2 min at 2000 rpm in a planetary mixer (Thinky ARV-310) at ambient pressure. Subsequently, the PFSA dispersion is added and mixed for 10 min at

Table I. Ink composition for the preparation of MPLs and final MPL compositions.

MPL	ink composition									MPL composition	
	Li400 carbon black [g]	VGCF-H carbon fibers [g]	Triton X-100 ¹ [g]	methyl cellulose [g]	DI Water [g]	1-propanol [g]	PTFE dispersion ² [ml]	PFSA dispersion ³ [ml]	solids content ⁴ [wt%]	VGCF content ⁵ [wt%]	binder content ⁶ [wt%]
0% VGCF hydrophobic	6.40	-	0.176	0.77	34.00	-	1.83	-	18	0	20
0% VGCF hydrophilic	6.40	-	-	-	-	29.50	-	6.63	18	0	20
50% VGCF hydrophobic	3.20	3.20	0.176	0.77	34.00	-	1.83	-	18	40	20
80% VGCF hydrophobic	1.28	5.12	0.176	0.77	34.00	-	1.83	-	18	64	20
80% VGCF hydrophilic	1.28	5.12	-	-	-	29.50	-	6.63	18	64	20
100% VGCF hydrophobic	-	6.40	0.176	0.77	34.00	-	1.83	-	18	80	20

¹For accurate admixture, an aqueous solution with 0.2 ml_{Triton X-100}/g_{solution} was used.

²3M Dyneon TF 5035GZ dispersion with 58wt% PTFE content.

³Low EW PFSA ionomer dispersion with 20wt% ionomer content.

⁴Content of carbon and PTFE/PFSA: $m_{\text{carbon+PTFE/PFSA}}/m_{\text{ink}}$.

⁵Prospected VGCF content in MPL, assuming only carbon and binder remain after the final heat treatment: $m_{\text{VGCF}}/m_{\text{carbon+PTFE/PFSA}}$.¹⁵

⁶Prospected binder (PTFE/PFSA) content in MPL assuming only carbon and binder remain after the final heat treatment: $m_{\text{PTFE/PFSA}}/m_{\text{carbon+PTFE/PFSA}}$.

500 rpm. Finally the ink is degassed under vacuum (30 kPa) at the same rotation speed for 2 min.

The coating is accomplished with 75 μm (80% VGCF) or 100 μm (0% VGCF) thick stencils and a doctor blade (analogously to the way described in Reference 15), followed by drying at 80°C for 30 min. In contrast to the PTFE containing coatings, a subsequent heat-treatment procedure at higher temperatures is not necessary, because: (i) the PFSA dispersion is free of additives, hence, no decomposition of unwanted substances is needed; and (ii) the polymer is highly dispersed in the 1-propanol rich solvent,⁵² which makes a higher temperature step to enable a flow of the polymer redundant. The thicknesses are measured as for hydrophobic coatings by applying Eq. 4.

Mercury intrusion porosimetry.—Mercury intrusion porosimetry measurements of hydrophobic GDL-S/MPL and hydrophobic free-standing MPL samples ($m_{\text{sample}} \approx 100 \text{ mg} - 300 \text{ mg}$) are conducted with two porosimeters (Pascal 140 and Pascal 440; CE Elantech, Inc. USA). For freestanding MPLs, the MPL porosity (ϵ_{MPL}) is calculated from the total cumulative pore volume normalized to the MPL mass v_{pore} (in units of $\text{mm}^3_{\text{pore}} \text{g}^{-1}_{\text{sample}}$) and the bulk MPL volume v_{MPL} (in units of $\text{mm}^3_{\text{pore}} \text{g}^{-1}_{\text{sample}}$) which is the sum of the MPL mass normalized pore volume (v_{pore}), the bulk volume of the carbon materials (carbon black and VGCF assuming bulk densities of $\rho_{\text{CB}} = 1.9 \text{ g cm}^{-3}$ and $\rho_{\text{VGCF}} = 2.0 \text{ g cm}^{-3}$) and of the bulk volume of the PTFE binder (using a bulk density of $\rho_{\text{PTFE}} = 2.16 \text{ g cm}^{-3}$).

$$\epsilon_{\text{MPL}} = \frac{v_{\text{pore}}}{v_{\text{MPL}}} = \frac{v_{\text{pore}}}{v_{\text{pore}} + \frac{w_{\text{CB}}}{\rho_{\text{CB}}} + \frac{w_{\text{VGCF}}}{\rho_{\text{VGCF}}} + \frac{w_{\text{PTFE}}}{\rho_{\text{PTFE}}}} \quad [5]$$

where w_{CB} , w_{VGCF} , and w_{PTFE} refer to the wt% of carbon and PTFE, respectively, in the MPL. The detailed procedure is described in Reference 15.

Scanning electron microscopy.—Images of carbon black, carbon fibers, and all prepared GDL-S/MPL samples (in top- and cross-sectional view) are taken by scanning electron microscopy (SEM). This was mostly done using a FESEM 7500F field emission SEM (JEOL) at acceleration voltages between 0.5 kV and 1.0 kV in the secondary electron imaging mode. For this, the carbon materials are immobilized on a carbon tape and loose particles are blown off. Images of the Li400 carbon black powder are taken at a magnification of x50,000 and images of VGCF at a magnification of x10,000. Top-view images of all prepared MPLs coated on the GDL-substrate were recorded at magnifications of x10,000 and x25,000. Furthermore, cross-sectional images are taken for hydrophobic 0% VGCF and the 100% VGCF MPLs coated on GDL-substrates at a magnification of x250. For that, the samples are prepared by bending the GDL until the MPL breaks

naturally and then fixing them in a cross-section sample holder (these images are shown in Figures 4e/4f and will be discussed later).

Finally, the MPLs coated on GDL-substrates with 0% VGCF and 100% VGCF are additionally examined in top- and cross-sectional view in a JCM-6000 benchtop SEM (JEOL) at 5 kV acceleration voltage and a magnification of x500 by the secondary electron detector. Images are shown in Figures 4a–4d. The cross-sectional samples are prepared by cutting the materials with a razor blade in order to create a clean cutting edge; subsequently the materials are fixed in a cross-section sample holder together with the top-view sample (these images, recorded as was done in Reference 15 are shown in Figures 4a–4d and will be discussed later).

Fuel cell test setup.—The fuel cell test assembly is identical to the one used in Reference 15. The most important specifications are summarized in Table II.

Fuel cell test procedures.—Fuel cell tests were conducted according to Ref. 15. Initial cell conditioning is performed by stepping the voltage under hydrogen (1390 nccm; 1 nccm \equiv 1 norm cubic centimeter per minute or 1 nml min^{-1} defined at 0°C and 1 atm, which corresponds to $7.43 \cdot 10^{-7} \text{ mol s}^{-1}$) and air (3320 nccm) at $T_{\text{cell}} = 80^\circ\text{C}$, $p_{\text{abs}} = 150 \text{ kPa}$, and 100% relative humidity (RH) in the following sequence: 0.6 V for 45 min, 0.95 V for 10 min, and 0.85 V for 5 min; this sequence is repeated ten times. Each investigated GDL-S/MPL type is measured two times in individually built cells; the error bars shown in the polarization curves, for the high frequency resistance (*HFR*) and for the oxygen transport resistances (R_{T,O_2}) represent the standard deviation from these two repeat experiments. Differential-flow H_2/air or $\text{H}_2/\text{dilute-air}$ (10% O_2 in N_2) polarization curves are recorded in potentiostatic mode by stepping the voltage from 0.9 V to 0.3 V (or in some cases 0.05 V) in steps of 50 mV after pre-conditioning the cell at 0.75 V for 15 min, followed by measuring the open circuit voltage (OCV). Each point is held for 10 min to reach steady-state and the shown data are averaged over the last 30 s at each voltage. Impedance spectra are recorded for each data point from 100 kHz to 10 Hz with a perturbation voltage of $\pm 10 \text{ mV}$, using the low noise setup of the hybrid impedance mode of the Gamry potentiostat; the *HFR* is extracted from the high-frequency intercept of the impedance data with the real axis in the associated Nyquist plots. High constant flow rates of 2000 nccm of hydrogen and 5000 nccm of either air or 10% O_2 in N_2 are applied in order to realize differential-flow conditions (stoichiometries for hydrogen and oxygen ≥ 10 at the highest current densities) at the operating conditions 1–3 listed in Table III.

Please consider that our here shown “dry operating conditions” at $T_{\text{cell}} = 80^\circ\text{C}$, $p_{\text{abs}} = 170 \text{ kPa}$, and $\text{RH} = 70\%$ with differential flows

Table II. Details of fuel cell test setup.

Property	Description
fuel cell setup	single cell with 5 cm ² active area (Fuel Cell Technologies)
flow fields	5 cm ² active area, 7 channels with 1 serpentine (Poco Graphite, see Ref. 51)
MEA	W. L. Gore & Associates, Primea Mesga A510.1/M715.18/C580.4
electrode loadings	anode: 0.1 mg _{Pt} cm ⁻² ; cathode: 0.4 mg _{Pt} cm ⁻²
GDLs	anode: commercial GDL-substrate w/ MPL (Freudenberg) cathode: commercial GDL-S/MPL (Freudenberg) or in-house prepared MPLs on the same commercial GDL-S
compression/gaskets	PTFE coated glass fabrics (FIBERFLON GmbH & Co. KG) on both electrodes at thicknesses in order to realize ≈20% GDL compression (details in Ref. 47)
fuel cell test station	custom-designed Greenlight Innovation G60 fuel cell test station
test equipment	load module: 120 A Agilent N3306A; potentiostat: Gamry Reference 3000

(hydrogen and air stoichiometries of ≥ 10) have been developed to result in no liquid water in the fuel cell, in order to investigate the hydrophobic/hydrophilic MPLs at low membrane humidification and in order to be comparable with “dry operating conditions” in single cell tests with stoichiometrically controlled hydrogen and air flows. For example, to achieve an average *RH* of 70% (arithmetic average value between inlet and outlet *RH*) at typical stoichiometries of 1.5 for hydrogen and 1.8 for air and at a cell pressure of 170 kPa_{abs}, the inlet *RH* would have to be approximately 24% considering a co-flow configuration (calculated by a gas and water vapor mass balance between inlet and outlet, and assuming an isothermal cell with negligible pressure drops).

For the measurement of the limiting current density, anode flow rates of 2000 nccm H₂ and cathode flow rates of 5000 nccm diluted oxygen in 10 different dry mole fraction ($x_{O_2, dry}$) between 0.5% and 28% are set. At each $x_{O_2, dry}$, the current densities obtained at 0.30 V, 0.15 V, 0.10 V, and 0.05 V are recorded by holding for 2 min to reach steady-state at each voltage and then averaging the measured current for 15 s. The total oxygen transport resistance (R_{T,O_2}) is calculated according to Eq. 2 and plotted vs. the limiting current density i_{lim} .

Morphology and Performance of Hydrophobic MPLs with Carbon Fibers

Morphology of carbon materials.—For the preparation of all MPLs in this study, two different carbon materials are used: Li400 carbon black (Denka) and vapor grown carbon fibers VGCF-H (Showa Denko). Figure 1 shows SEM images of both materials at different magnifications to capture their dimensional extension. The acetylene black (Figure 1a) consists of carbon black particles, which clearly have widely varying diameters between 20 nm and 300 nm. While the manufacturer provides a mean diameter of 48 nm, Figure 1a shows that the primary particles have a wide range of particle sizes; assuming dense spherical primary carbon particles with a density of ≈ 1.9 g cm⁻³, our measured BET area of ≈ 37 m² g⁻¹¹⁵ would yield an average particle

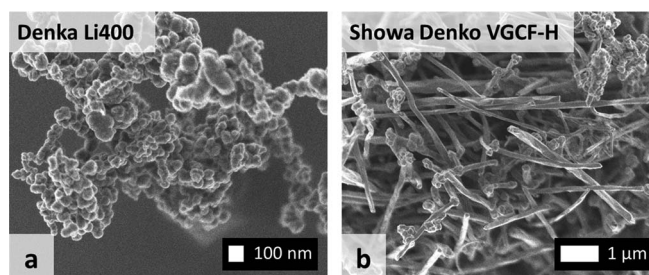
size of ≈ 85 nm. This means that some large particles with > 100 nm in diameter must consist of several fused smaller primary particles. All primary particles agglomerate to larger secondary structures of several 100 nm in size, which have different shapes from chains to bulky spheres.

The VGCF-H carbon fibers are shown in Figure 1b. While we measure fiber lengths of mostly < 10 μ m, the manufacturer specifies 10–20 μ m. On the other hand, the measured fiber diameters in the range of ≈ 70 –200 nm fit well with the manufacturer specification of ≈ 150 nm. Although the SEM image in Figure 1b is made from the pure VGCF-H fibers, some spherical particles and particle agglomerates can be observed, which are adhered to the fibers. Contrary to the rather bulky structures of the Li400 carbon black, the VGCF-H material consist of long carbon fibers, which are on the order of magnitude of the MPL thickness of 30 ± 5 μ m. This completely different morphology of the VGCF-H fibers is thus expected to significantly affect the MPL structural properties, which is why we decided to utilize these two materials. Note that furtheron, VGCF-H will be referred to as VGCF for simplicity.

Structural characterization of GDLs and MPLs.—In the following, we analyze freestanding MPLs and the respective MPLs coated on GDL-substrates by SEM imaging in order to investigate their structural properties (Figure 2 and Figure 4) as well as by mercury porosimetry to determine porosities and pore size distributions of the porous materials (Figure 3 and Figure 5). For MPLs with hydrophobic PTFE binder (for compositions see Table I), VGCF contents of 0% (pure carbon black, Figures 2a/2b), 50% (Figures 2e/2f), 80% (Figures 2g/2h), and 100% (i.e., only VGCF, Figures 2k/2l) are realized. The SEM top-view images of these MPLs (from the final GDL-S/MPL samples) are shown in Figure 2. The structures of the materials which consist of only one carbon component (0% and 100% VGCF MPLs) are determined by the carbon component itself. The pure carbon black based MPL (0% VGCF MPL, Figures 2a/2b) shows rather small pores, resulting from the carbon black secondary agglomerate structure; on the other hand, the pure VGCF based MPL (100% VGCF MPL, Figures 2k/2l) is dominated by the structure-forming carbon fibers, which create a pore

Table III. Fuel cell test conditions, with the same conditions being applied to anode and cathode. Cell pressures are always given as absolute pressures measured at the cell inlet.

N°	Name	T_{cell} [°C]	p_{abs} [kPa]	<i>RH</i> [%]	Figures
1	dry ^{1,2}	80	170	70	Figure 7, Figure 12
2	humid ^{1,2}	50	300	120	Figure 8, Figure 13
3	normal ^{1,2,3,4}	80	300	100	Figure 9, Figure 10
4	transition ¹	50	400	77	Figure 6, Figure 11

¹measurement of the limiting current density.²differential-flow H₂/air polarization curves in air.³differential-flow polarization curves with H₂ and 10% O₂/N₂.⁴only measured for the hydrophobic commercial MPL, the 0% VGCF MPL, and the 100% VGCF MPL.**Figure 1.** Scanning electron microscopy images of (a) Denka Li400 carbon black with a magnification of x50,000, and (b) Showa Denko VGCF-H carbon fibers with a magnification of x10,000.

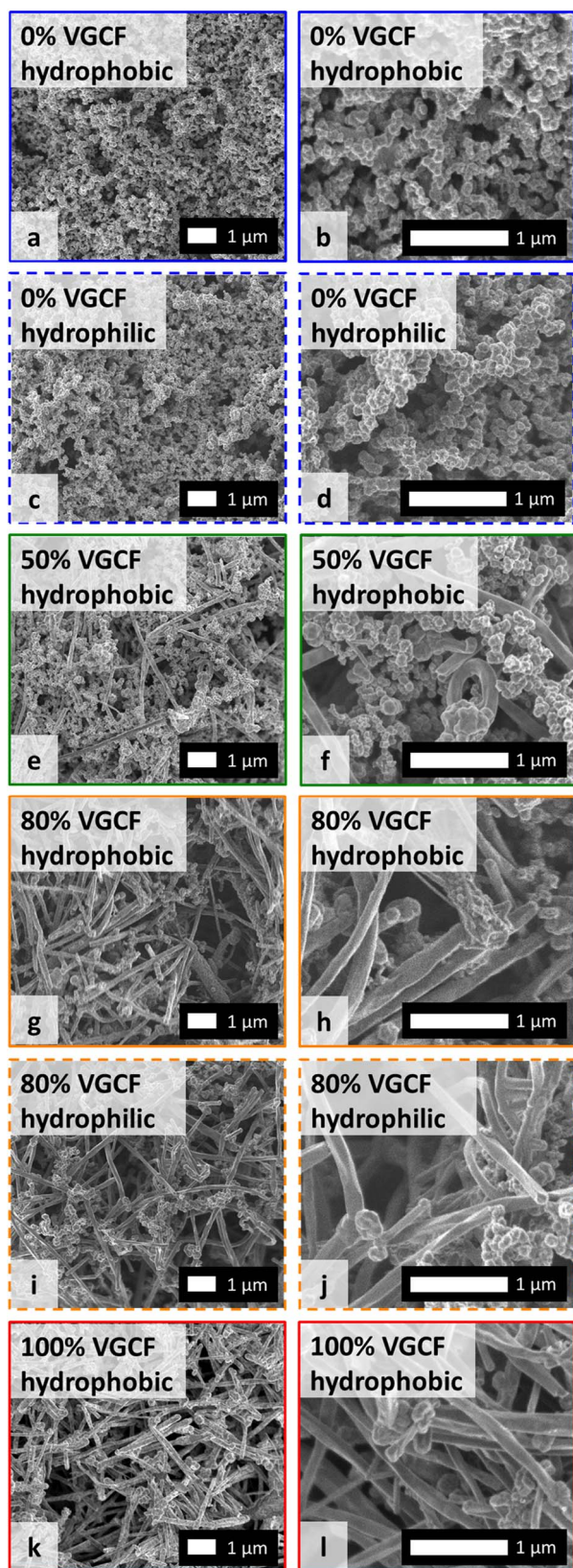


Figure 2. SEM top-view images of the MPL side of GDL-S/MPL samples for fuel cell testing showing hydrophobic and hydrophilic MPLs with: (a,b) 0% VGCF and PTFE binder, (c,d) 0% VGCF and PFSA binder, (e,f) 50% VGCF and PTFE binder, (g,h) 80% VGCF and PTFE binder, (i,j) 80% VGCF and PFSA binder, and (k,l) 100% VGCF and PTFE binder. Magnifications are $\times 10,000$ (a,c,e,g,i,k) and $\times 25,000$ (b,d,f,h,j,l). Images of 0% VGCF MPL are taken from Ref. 15.

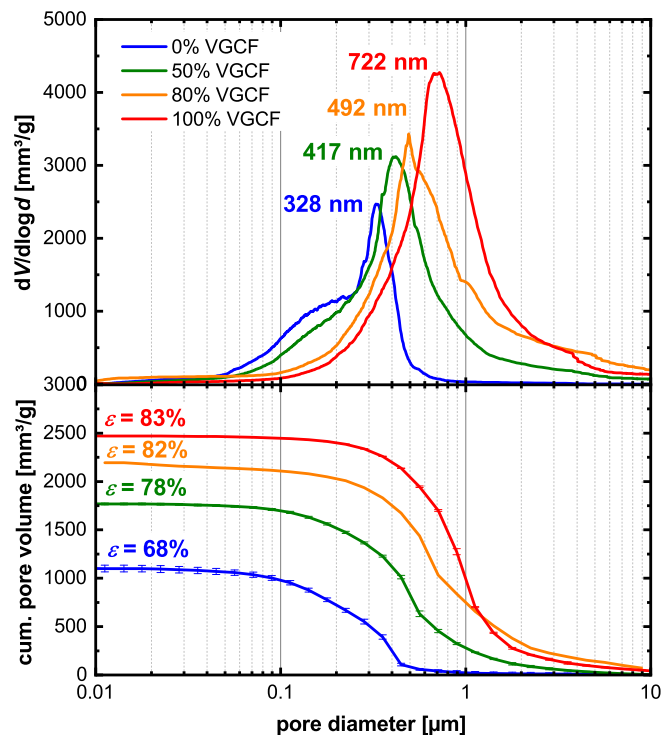


Figure 3. Mass-normalized cumulative pore volume (lower panel) and differential pore volume $dV/d\log d$ (upper panel) as function of pore diameter for freestanding hydrophobic MPLs with 0% VGCF (blue lines), 50% VGCF (green lines), 80% VGCF (orange lines), and 100% VGCF (red lines), all using PTFE binder (for compositions see Table 1). Porosities ϵ [%] obtained from the cumulative pore volumes (v_{pore}) using Eq. 5 and the PSD-maxima [nm] are referred in the graph. Data of 0% VGCF MPL are taken from Ref. 15.

network with clearly larger pores and an apparently higher porosity. The small particles which are visible for the 100% VGCF MPL in Figures 2k/2l are also visible in the as-received fiber material in Figure 1b, so that it must originate from the fiber rather than from the MPL production. The 50% and 80% VGCF MPLs (Figures 2e–2h) appear as expected like mixtures of the pure materials. Qualitatively, the SEM images suggest an increase of pore size and porosity with increasing VGCF content. Interestingly, while all MPLs contain 20wt% of PTFE (corresponding to $\approx 20\text{vol.}\%$ PTFE), there are no PTFE particles visible any of the in-lab prepared MPLs compared to the commercial MPL (as was shown in Fig. 3b of Ref. 15). This indicates that the PTFE is finely dispersed, presumably as a thin film within the MPL, as previously shown.¹⁵

By mercury porosity measurements a quantification of the pore size distribution and the porosities is achievable for the MPL when using freestanding MPLs (i.e., w/o GDL-substrate). Figure 3 shows the differential mass-normalized pore volume $dV/d\log d$ in the upper graph and the cumulative mass-normalized pore volume in the lower graph. All MPLs have pore sizes in the range from 50 nm to 10 μm , except for the 0% VGCF MPL (blue line) for which the largest pores are only ≈ 800 nm and which has the smallest PSD-maximum of 328 nm, as reported previously.¹⁵ With increasing VGCF content of 50% (green line), 80% (orange line) and 100% (red line), the pore size distribution broadens and is shifting toward larger pore sizes, with PSD-maxima of 417 nm, 492 nm, and 722 nm. At the same time, the total cumulative pore volume of the MPLs (v_{pore}) is increasing with increasing VGCF content, from 1100 $\text{mm}^3 \text{g}^{-1}$ for 0% VGCF to 2470 $\text{mm}^3 \text{g}^{-1}$ for 100% VGCF. Using Eq. 5, this corresponds to an increase in porosity from 68% for 0% VGCF, to 78% for 50% VGCF, to 82% for 80% VGCF, and finally to 83% for 100% VGCF. Thus, the quantitative porosity results from mercury intrusion measurements on freestanding MPLs confirm the impression from the SEM images in Figure 2, which qualitatively

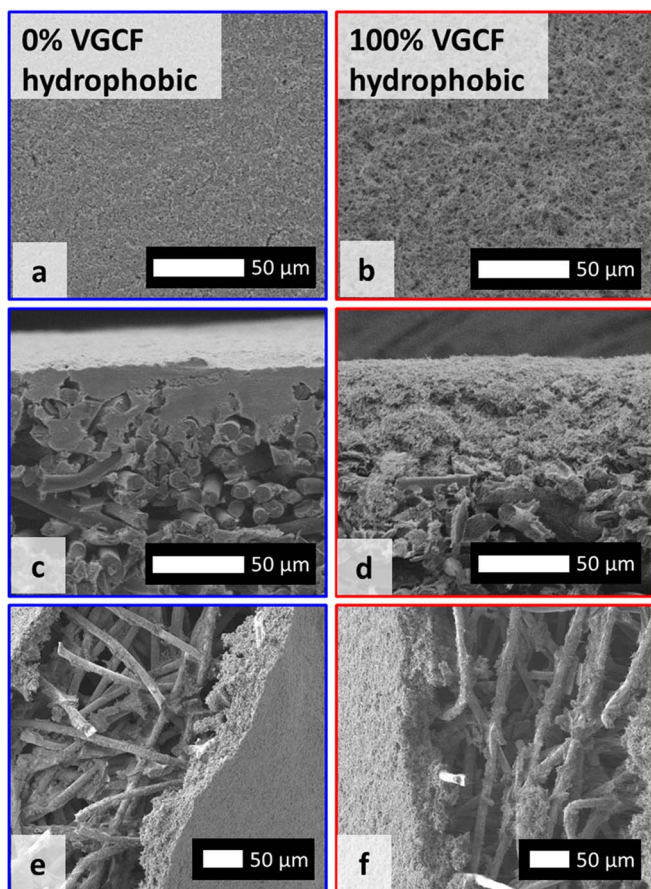


Figure 4. Scanning electron microscopy images of GDL-S/MPL samples for fuel cell testing composed of MPLs with (a,c,e) 0% VGCF and PTFE binder, and (b,d,f) 100% VGCF and PTFE binder. Images show top-views of the MPLs with magnification of $\times 500$ (a,b) as well as cross-sectional views prepared either by cutting with a magnification of $\times 500$ (c,d; MPL on top) or by bending the samples with a magnification of $\times 250$ (e,f). Images of 0% VGCF MPL are taken from Ref. 15.

indicated an increase in pore size and porosity for an increasing VGCF content.

SEM images of the hydrophobic GDL-S/MPL samples used for electrochemical testing are shown in Figure 4 for 0% VGCF (a,c,e) and 100% VGCF (b,d,f), with top-views of the MPLs (a,b) and in also in cross-sectional views produced either by cutting (c,d) or by bending the samples (e,f). In the top-view of the MPL images at a magnification of $\times 500$, no macroscopic cracks are observed in neither the 0% VGCF MPL (a) nor in the 100% VGCF MPL (b). Nevertheless, even at these low magnifications, we can see in both the top-view (a,b) and the cross-sectional view (c,d) the dense structure of the pure carbon black MPL (a,c) compared to the fluffy structure of the 100% VGCF MPL (b,d). For both MPLs, distinct intrusion of the MPL into the GDL substrate is observed. Despite the length of the VGCF fibers of up to $10\ \mu\text{m}$, these imbibe snugly into the larger pore structure of the GDL-substrate with pore sizes of around $30\ \mu\text{m}$. From the MPL cross-sectional images obtained by bending the samples (Figures 4e/4f), one can get an impression about the adhesive interaction between MPL and GDL substrate: when applying mechanical bending stress, the MPL is breaking, while the rather robust GDL-substrate still remains intact. Even though the MPL is breaking, it still adheres to the GDL-substrate. At the position, which becomes free of the MPL layer, there are still particles of carbon black or VGCF left sticking to the GDL-substrate, indicating that the carbon/PTFE composite has a very strong contact to the GDL-substrate and that the MPL exhibits a high mechanical stability.

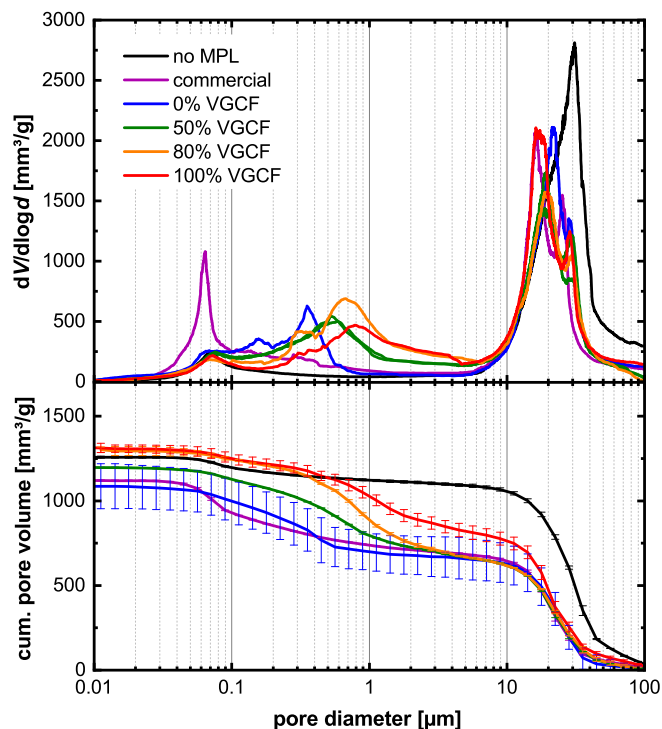


Figure 5. Mass-normalized cumulative pore volume (bottom) and differential pore volume $dV/d\log d$ (top) as function of pore diameter measured by mercury intrusion porosimetry for the Freudenberg GDL-substrate w/o MPL (black lines) and for the hydrophobic (20wt% PTFE) GDL-S/MPL samples based on the same substrate coated with the following MPLs: commercial MPL (purple lines), MPLs with 0% VGCF (blue lines), with 50% VGCF (green lines), with 80% VGCF (orange lines), and 100% with VGCF (red lines). Data of the 0% VGCF MPL, the commercial MPL, and for GDL-substrate without MPL are taken from Ref. 15.

To investigate the interaction between MPL and GDL-substrate, Figure 5 is showing the results of mercury intrusion porosimetry of the different GDL-S/MPL samples, with MPLs coated onto the same GDL-S, including a commercial MPL and the GDL-substrate without MPL (details see also Ref. 15). The substrate without MPL (“no MPL”, black line) is showing one large peak at $\approx 30\ \mu\text{m}$ containing most of the pore volume. Additionally it exhibits another small peak at $\approx 70\ \text{nm}$, which presumably originates from a carbon containing impregnation of the GDL-substrate.¹⁵ If an MPL is coated onto the GDL-substrate, its pore size distribution is shifted toward smaller pore sizes, with a now lower PSD-maximum of $\approx 20\ \mu\text{m}$, likely due to the filling of large pores by the intruding MPL.¹⁵

As outlined before, pore sizes of the MPL are registered in the range of up to $10\ \mu\text{m}$. The purple line reveals the data from the commercial GDL-S/MPL (same data as in Ref. 15), with a second PSD-maximum at $64\ \text{nm}$ from the MPL, which constitutes the MPL with the smallest pores in the present study. The 0% VGCF MPL shows a PSD-maximum at $353\ \text{nm}$ (freestanding MPL: $328\ \text{nm}$), the 50% VGCF MPL at $586\ \text{nm}$ (freestanding MPL: $417\ \text{nm}$), the 80% VGCF MPL at $671\ \text{nm}$ (freestanding MPL: $492\ \text{nm}$), and the 100% VGCF MPL at $782\ \text{nm}$ (freestanding MPL: $722\ \text{nm}$). The pore sizes follow the same trend as for the freestanding MPLs (see Figure 3), with an increase in pore size with increasing VGCF content. It should be noted that the PSD-maxima ascribed to the MPL when referencing the data in Figure 5 to the MPL weight are slightly smaller in case of the coated MPLs. However, one has to state that the absolute MPL volume in case of the GDL-S/MPL samples is significantly smaller than for the equivalent freestanding MPL, and also that the MPL features in the PSD partially overlap with those of the GDL-substrate at $\approx 70\ \mu\text{m}$, which is why the data in the relevant pore size range is not so clear as for the freestanding MPLs in Figure 3. Also, the total cumulative pore

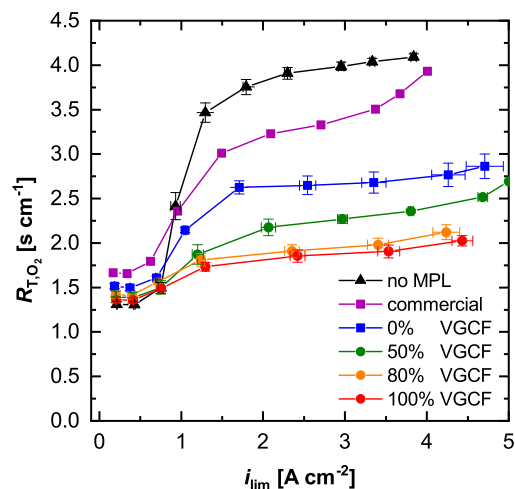


Figure 6. R_{T,O_2} as function of limiting current density under transition conditions for the Freudenberg GDL-substrate with no MPL (black) and with the following hydrophobic cathode MPLs coated on the same substrate: commercial MPL (purple), 0% VGCF (blue), 50% VGCF (green), 80% VGCF (orange), and 100% VGCF (red), with PTFE as binder. Operating conditions are $T_{cell} = 50^\circ\text{C}$, $RH = 77\%$, $p_{abs} = 400\text{ kPa}$; i_{lim} was measured for various dry oxygen contents ($x_{O_2,dry}$) between 0.5% and 28%. Data of 0% VGCF MPL, commercial MPL and no MPL are taken from Reference 15. The error bars represent the standard deviation of from two independently measured cells.

volumes (Figure 5, lower graph) do not follow the trend of the free-standing MPLs in Figure 3, because in the present case the cumulative pore volume is dominated by the larger portion of the GDL-substrate.

Oxygen transport resistance and fuel cell performance.—To analyze the oxygen transport properties at dry and humid conditions, the oxygen transport resistance was determined via the limiting current density at various dry oxygen contents ($x_{O_2,dry}$) in the cathode feed gas. Figure 6 shows the total oxygen transport resistance (R_{T,O_2}) versus the limiting current density (i_{lim}) at conditions where a transition from a dry to a water saturated diffusion medium is observable ($T_{cell} = 50^\circ\text{C}$, $RH = 77\%$, $p_{abs} = 400\text{ kPa}$). At small limiting current densities of $i_{lim} < 0.5\text{ A cm}^{-2}$, obtained with $x_{O_2,dry}$ of 0.5% and 1.0%, the GDL, the MPL, and the cathode electrode do not contain liquid water and R_{T,O_2} is constant at a low level. At elevated current densities, liquid water is condensing inside the pores of the GDL-S/MPL and the cathode electrode, causing a partial blockage of gas diffusion pathways. This leads to an increase of R_{T,O_2} until a maximum level of water saturation at $>2\text{ A cm}^{-2}$ is reached for all MPLs.

In the dry region, the GDL without MPL (“no MPL”, black symbols) has the smallest R_{T,O_2} of 1.3 s cm^{-1} due to the absence of the additional diffusion resistance imposed by the MPLs. As already shown in our previous study, the GDL with the commercial MPL (purple symbols), which is thicker ($\approx 50\text{ }\mu\text{m}$) and has a lower effective diffusivity,¹⁵ shows the highest dry R_{T,O_2} of $\approx 1.7\text{ s cm}^{-1}$. On the other hand, the thinner 0% VGCF MPL (blue line) has a distinctly smaller dry R_{T,O_2} ; the addition of VGCF further reduces R_{T,O_2} , but the curves of 50%, 80%, and 100% VGCF (green/orange/red lines) are actually overlapping in the dry region.

In the region where the porous layers have reached their water saturation level, obtained at $i_{lim} > 2\text{ A cm}^{-2}$, more significant differences can be observed. A GDL-substrate without MPL is known to flood immediately at the interface between GDL and cathode if liquid water is present, which leads to a severe increase of oxygen transport resistance and to high R_{T,O_2} .^{3,15,47} The presence of the commercial MPL reduces R_{T,O_2} at humid conditions significantly. Applying the 0% VGCF MPL, a further reduction to a level of $R_{T,O_2} \approx 2.6\text{ s cm}^{-1}$ is achieved. By replacing the carbon black with a VGCF containing MPL, the oxygen transport can be decreased to a level of $\approx 2.3\text{ s cm}^{-1}$ (50% VGCF), $\approx 2.0\text{ s cm}^{-1}$ (80% VGCF), and $\approx 1.9\text{ s cm}^{-1}$ (100% VGCF). This cor-

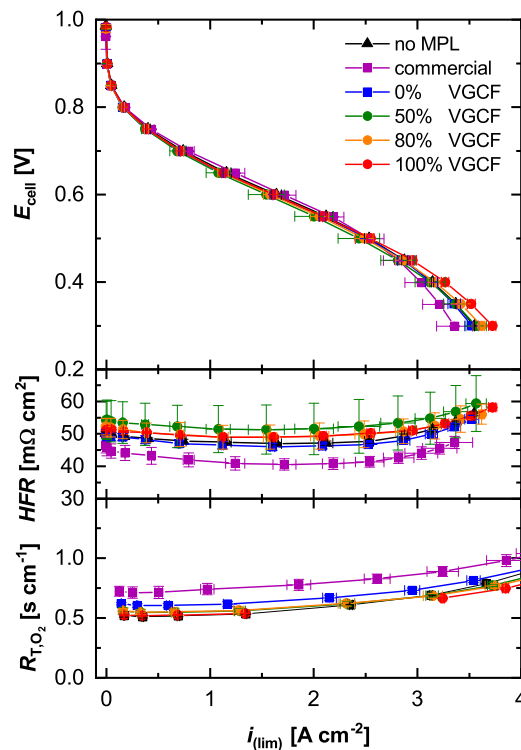


Figure 7. Differential-flow H_2/air polarization curves under dry conditions ($T_{cell} = 80^\circ\text{C}$, $RH = 70\%$, $p_{abs} = 170\text{ kPa}$) showing cell voltage (E_{cell} , top) and high frequency resistance (HFR , middle) versus current density (i) as well as total oxygen transport resistance (R_{T,O_2} , bottom) versus the limiting current density (i_{lim}) for the GDL-substrate with no MPL (black) and the following hydrophobic cathode MPLs coated on the same GDL-substrate: commercial MPL (purple), 0% VGCF MPL (blue), 50% VGCF MPL (green), 80% VGCF MPL (orange), and 100% VGCF MPL (red), with PTFE as binder. The limiting current density is measured for various dry oxygen contents ($x_{O_2,dry}$) between 0.5% and 28%. The error bars represent the standard deviation of two independently measured cells. Data of the 0% VGCF MPL, the commercial MPL, and no MPL are taken from Reference 15.

responds to a reduction of R_{T,O_2} by $\approx 25\%$ comparing the 0% VGCF with the 100% VGCF MPL.

These findings significantly affect the differential-flow H_2/air performance particularly at humid (Figure 8) and normal conditions (Figure 10) where liquid water is present in the diffusion medium, while the performance impact under dry conditions is minor (Figure 7). The latter is illustrated for the dry operating conditions ($T_{cell} = 80^\circ\text{C}$, $RH = 70\%$, $p_{abs} = 170\text{ kPa}$) in Figure 7, with the cell voltage (E_{cell} ; top panel) and the high frequency resistance (HFR ; middle panel) plotted versus the current density (i) as well as with the oxygen transport resistance (R_{T,O_2}) plotted versus the limiting current density (i_{lim}). Here, the H_2/air polarization curves of all tested materials are indeed very similar, with a current of around 1.6 A cm^{-2} at a cell voltage of 0.6 V. The associated HFR values at the open circuit voltage (OCV) range from 40–55 $\text{m}\Omega\text{ cm}^2$, then decrease slightly with increasing current density due to a humidification of the membrane, and finally increase at current densities of $>2\text{ A cm}^{-2}$ due to membrane dry-out as explained in Reference 15. The R_{T,O_2} values for all materials are at a very low level between 0.5 s cm^{-1} and 0.75 s cm^{-1} , increasing very little with increasing i_{lim} , which is consistent with the expectation that the under these dry conditions the porous media remain free of liquid water at all limiting current densities and that no water condensation is taking place.

The essentially identical cell voltage at 1.6 A cm^{-2} suggests that the O_2 transport induced losses must be negligible under dry conditions, which is indeed consistent with the O_2 transport induced voltage losses

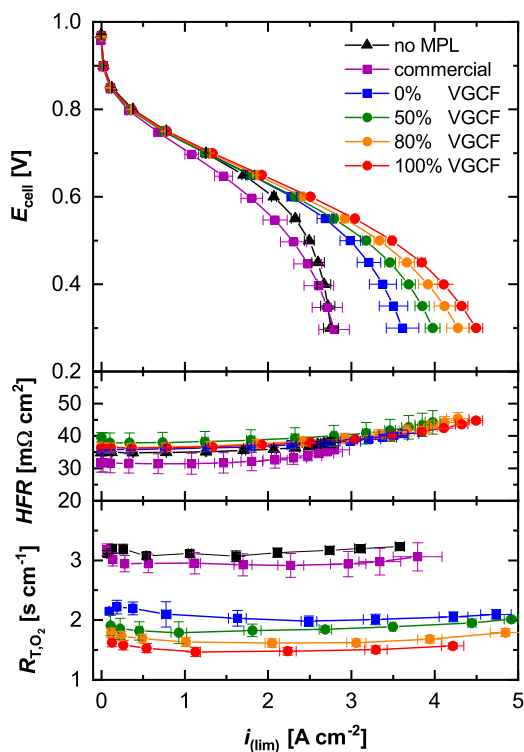


Figure 8. Differential-flow H_2/air polarization curves at humid conditions ($T_{\text{cell}} = 50^\circ\text{C}$, $RH = 120\%$, $p_{\text{abs}} = 300\text{ kPa}$) showing cell voltage (E_{cell} , top) and high frequency resistance (HFR , middle) versus current density (i) as well as total oxygen transport resistance (R_{T,O_2} , bottom) versus the limiting current density (i_{lim}) for the GDL-substrate with no MPL (black) and the following hydrophobic cathode MPLs coated on the same GDL-substrate: commercial MPL (purple), 0% VGCF MPL (blue), 50% VGCF MPL (green), 80% VGCF MPL (orange), and 100% VGCF MPL (red), with PTFE as binder. The limiting current density is measured for various dry oxygen contents ($x_{\text{O}_2,\text{dry}}$) between 0.5% and 28%. The error bars represent the standard deviation of two independently measured cells. Data of the 0% VGCF MPL, the commercial MPL, and no MPL are taken from Reference 15.

of $\Delta U_{\text{O}_2-\text{tx}} \approx 7\text{--}11\text{ mV}$ calculated for $i = 1.6\text{ A cm}^{-2}$ according to:⁵³

$$\Delta U_{\text{O}_2-\text{tx}} = \frac{RT}{F} \cdot \left(\frac{1}{4} + \frac{\gamma}{\alpha} \right) \cdot \ln \left(\frac{p_{\text{O}_2,\text{channel}} - \frac{RT}{4F} \cdot R_{\text{T},\text{O}_2} \cdot i}{p_{\text{O}_2,\text{channel}}} \right) \quad [6]$$

where R is $8.314\text{ J mol}^{-1}\text{ K}^{-1}$, F is the Faraday constant, γ is the ORR reaction order with respect to oxygen partial pressure ($\gamma = 0.75$), α is the effective transfer coefficient for the oxygen reduction reaction ($\alpha = 1$), and $p_{\text{O}_2,\text{channel}}$ is the O_2 partial pressure in the flow field channel of $p_{\text{O}_2,\text{channel}} \approx 28\text{ kPa}$ (based on a cathode pressure of $170\text{ kPa}_{\text{abs}}$, an O_2 concentration of 21%, and a water vapor pressure of $\approx 33\text{ kPa}$ at 80°C and 70% RH). Hence, at conditions where no liquid water is present in the diffusion medium, the impact of the MPL for a given GDL-substrate at relevant cell voltages is rather negligible.

This is very different for the differential-flow H_2/air performance at humid conditions ($T_{\text{cell}} = 50^\circ\text{C}$, $RH = 120\%$, $p_{\text{abs}} = 300\text{ kPa}$; see Figure 8), at which a significant fraction of liquid water saturation in the GDL-S/MPL occurs. At 0.6 V, the hydrophobic 0% VGCF MPL based on carbon black reaches a current density of 2.3 A cm^{-2} (blue symbols/lines), which is an enhancement compared to the GDL-substrate without MPL of 2.1 A cm^{-2} (black symbols/lines). Due to the higher thickness ($\sim 50\text{ }\mu\text{m}$ compared to $30\text{ }\mu\text{m}$ in-lab prepared MPLs) and lower effective diffusivity (smaller pore sizes, see Figure 5), both reflected by the significantly higher oxygen transport resistance (1.5–2 times higher compared to the in-lab prepared MPLs), the GDL with the commercial MPL even undercuts this performance with a current density of 1.8 A cm^{-2} (purple symbols/lines). The higher oxygen transport

resistance even cannot be compensated by the $\sim 10\text{ m}\Omega\text{ cm}^2$ lower HFR (a more detailed analysis can be found in Reference 15). With increasing VGCF content, however, we are able to increase the current density to 2.5 A cm^{-2} for 100% VGCF (red symbols/lines). The HFR s at OCV vary between $32\text{--}40\text{ }\Omega\text{ cm}^2$, with the commercial MPL showing the lowest value, at high current densities of $>2\text{ A cm}^{-2}$ and the accompanying lower efficiencies, the HFR also at the humid conditions increases slightly by 25%, presumably due to membrane dry-out. The reason for the superior performance of the hydrophobic VGCF based MPLs is the oxygen transport resistance: the higher the VGCF content, the lower becomes R_{T,O_2} . In the present case the GDL-S/MPL contains large amounts of liquid water already at the lowest current densities due to the over-humidified reactant feeds (120% RH) which result in the condensation of water in the porous layers. The constant level of R_{T,O_2} with constant values independent from the limiting current density indicates that the water saturation within the layers does not change significantly with current density, so that the effective O_2 diffusivity remains essentially constant. By using VGCF in the MPL, R_{T,O_2} can be effectively reduced by $\approx 29\%$ from $\approx 2.1\text{ s cm}^{-1}$ for 0% VGCF to $\approx 1.5\text{ s cm}^{-1}$ for 100% VGCF. The GDL-substrate without MPL and with the commercial MPL are at significantly higher levels of $\approx 3.0\text{--}3.1\text{ s cm}^{-1}$, analogous to what was already observed in Figure 6.

To see how the materials perform at operating conditions relevant for automotive applications, we measured differential-flow polarization curves, high frequency resistances, and limiting current densities at $T_{\text{cell}} = 80^\circ\text{C}$, $RH = 100\%$, $p_{\text{abs}} = 300\text{ kPa}$ in both air (simulating the stack inlet) as well as in 10% O_2 in N_2 (simulating the oxygen concentration at the stack outlet at an oxygen stoichiometry of 1.75).⁵⁴ The results for the cathode GDL-substrates with the hydrophobic commercial MPL, the 0% VGCF MPL, and the 100% VGCF MPL are shown in Figure 9 (10% O_2 in N_2) and in Figure 10 (air, i.e., 21% O_2). The performances at 0.6 V in either 10% O_2/N_2 or air are 1.5 A cm^{-2} and 2.2 A cm^{-2} for the commercial MPL, 2.1 A cm^{-2} and 3.1 A cm^{-2} for the 0% VGCF MPL, and 2.3 A cm^{-2} and 3.3 A cm^{-2} for the 100% VGCF MPL, respectively. The corresponding high frequency resistances are all at $\approx 30\text{ m}\Omega\text{ cm}^2$ and show an increase at current densities $>2\text{ A cm}^{-2}$ for 10% O_2 and $>4\text{ A cm}^{-2}$ for air, where the efficiency of the cell decreases and the heat release increases. This also indicates membrane dry-out as discussed before.

The oxygen transport resistances shows a similar trend as at humid conditions (see Figure 8), where the commercial MPL exhibits a higher R_{T,O_2} of 1.2 s cm^{-1} compared to the 0% and 100% VGCF MPLs with a rather similar R_{T,O_2} of $\approx 0.9\text{ s cm}^{-1}$. As shown in Reference 15 for the same or similar GDL materials at an identical point of operation, the GDL substrate, MPL, and cathode electrode are free of liquid water, so the oxygen transport resistance, which also in the present case is essentially constant over the whole range of i_{lim} , is only determined by the structural properties of the materials. Hence, the effective diffusivity of oxygen through the dry porous layers determines R_{T,O_2} .

Morphology and Performance of Hydrophobic vs. Hydrophilic MPLs

Characterization of hydrophilic MPLs.—For preparing hydrophilic MPLs, we replace the hydrophobic PTFE binder with a hydrophilic PFSA ionomer as a binder, a polymeric acid consisting of a fluorinated backbone polymer functionalized with sulfonic acid groups.⁵⁵ This material absorbs water and effectively reduces the contact angle θ (see Eq. 1).^{35,56,57} Because PFSA already starts to decompose at temperatures of $\approx 300^\circ\text{C}$ in air^{58,59} as compared to PTFE with decomposition temperatures of $>400^\circ\text{C}$, it is not possible to perform a temperature treatment to $>300^\circ\text{C}$, which would be necessary in order to decompose Triton X-100 and methylcellulose.¹⁵ Hence, an alternative preparation procedure is developed with 1-propanol as a solvent, in which the carbon components are well dispersible without additional stabilizers or thickeners (see Table I). We prepare hydrophilic MPLs with 0% VGCF (Figures 2c/2d) and 80% VGCF (Figures 2i/2j) in

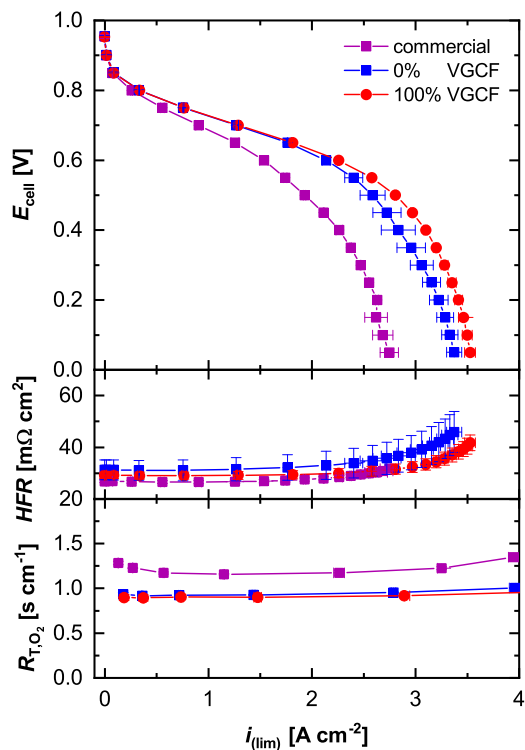


Figure 9. Differential-flow polarization curves under **normal conditions** relevant for automotive applications ($T_{\text{cell}} = 80^\circ\text{C}$, $RH = 100\%$, $p_{\text{abs}} = 300$ kPa) with H_2 and 10% O_2 in N_2 to mimic the stack outlet conditions showing cell voltage (E_{cell} , top) and high frequency resistance (HFR , middle) versus current density (i) as well as total oxygen transport resistance (R_{T,O_2} , bottom) versus the limiting current density (i_{lim}) for the following hydrophobic cathode MPLs coated on the same Freudenberg GDL-substrate: commercial MPL (purple), 0% VGCF MPL (blue), and 100% VGCF MPL (red), with PTFE as binder. The limiting current density is measured for various dry oxygen contents ($x_{\text{O}_2,\text{dry}}$) between 0.5% and 28%. The error bars represent the standard deviation of two independently measured cells. Data of 0% VGCF MPL and commercial MPL are taken from Ref. 15.

order to create a significant structural contrast. These materials can be compared to the hydrophobic MPLs with the same carbon composition namely 0% VGCF (Figures 2a/2b) and 80% VGCF (Figures 2g/2h). The morphology of the hydrophilic and hydrophobic MPLs are indistinguishable in the SEM images. For 0% VGCF, the more dense structure is dominated by the carbon black, while for 80% VGCF the carbon framework is defined by the carbon fibers and only few carbon black particles are observed in the SEM images. Even though the hydrophobic and hydrophilic MPLs are prepared by different procedures and with ink compositions (see Experimental section), the morphology of the resulting MPLs are very similar, so that their main differences are expected to be due to differences in their hydrophilicity.

Oxygen transport and fuel cell performance of hydrophilic/hydrophobic MPLs.—The oxygen transport resistance R_{T,O_2} for hydrophilic MPLs is investigated at $T_{\text{cell}} = 50^\circ\text{C}$, $RH = 77\%$, $p_{\text{abs}} = 400$ kPa, the same condition at which the hydrophobic MPLs were first evaluated (Figure 6). The data for the hydrophilic MPLs (open symbols) with 0% VGCF (blue lines/symbols) and 80% VGCF (orange lines/symbols) are plotted in Figure 11 together with the correspondent hydrophobic MPLs (full symbols) of the same carbon composition (same data as in Figure 6). At small limiting current densities of $i_{\text{lim}} < 0.5$ A cm^{-2} , obtained with $x_{\text{O}_2,\text{dry}}$ of 0.5% and 1.0%, the GDL-S/MPLs do not contain liquid water and the measured oxygen transport resistances are very similar with ≈ 1.5 s cm^{-1} for all four MPLs, with the 80% VGCF MPLs showing slightly smaller R_{T,O_2} values as was observed also in Figure 6. This is

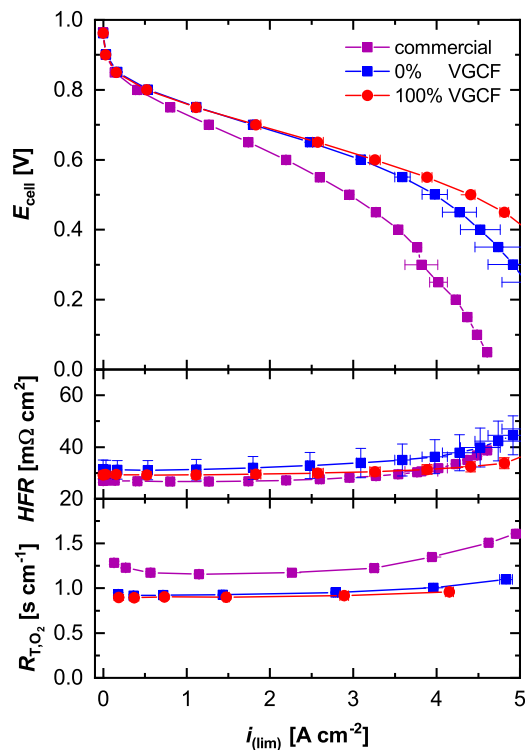


Figure 10. Differential-flow H_2/air polarization curves under **normal conditions** relevant for automotive applications ($T_{\text{cell}} = 80^\circ\text{C}$, $RH = 100\%$, $p_{\text{abs}} = 300$ kPa) with H_2/air to mimic the stack inlet conditions showing cell voltage (E_{cell} , top) and high frequency resistance (HFR , middle) versus current density (i) as well as total oxygen transport resistance (R_{T,O_2} , bottom) versus the limiting current density (i_{lim}) for the following hydrophobic cathode MPLs coated on the same Freudenberg GDL-substrate: commercial MPL (purple), 0% VGCF MPL (blue), and 100% VGCF MPL (red), with PTFE as binder. The limiting current density is measured for various dry oxygen contents ($x_{\text{O}_2,\text{dry}}$) between 0.5% and 28%. The error bars represent the standard deviation of two independently measured cells. Data of the 0% VGCF MPL and the commercial MPL are taken from Reference 15.

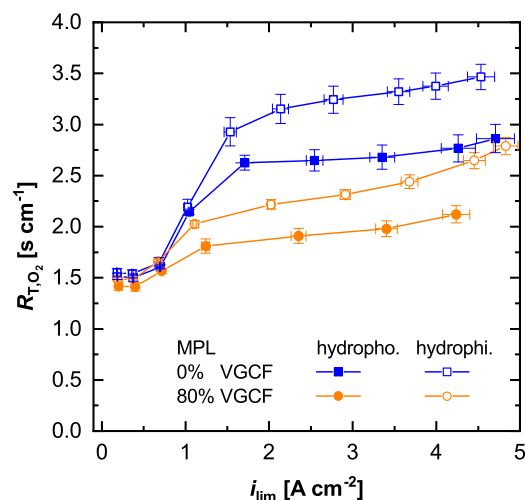


Figure 11. R_{T,O_2} as function of limiting current density under **transition conditions** for the following MPLs coated on the Freudenberg GDL-substrate: 0% VGCF with hydrophobic PTFE (blue line, full squares) or hydrophilic PFSA (blue line, empty squares) as binder, and 80% VGCF with PTFE (orange line, full squares) or PFSA (orange line, empty squares) as binder. Operating conditions are $T_{\text{cell}} = 50^\circ\text{C}$, $RH = 77\%$, $p_{\text{abs}} = 400$ kPa; i_{lim} was measured for various dry oxygen contents ($x_{\text{O}_2,\text{dry}}$) between 0.5% and 28%. Data of the hydrophobic 0% VGCF MPL is taken from Reference 15. The error bars represent the standard deviation of from two independently measured cells.

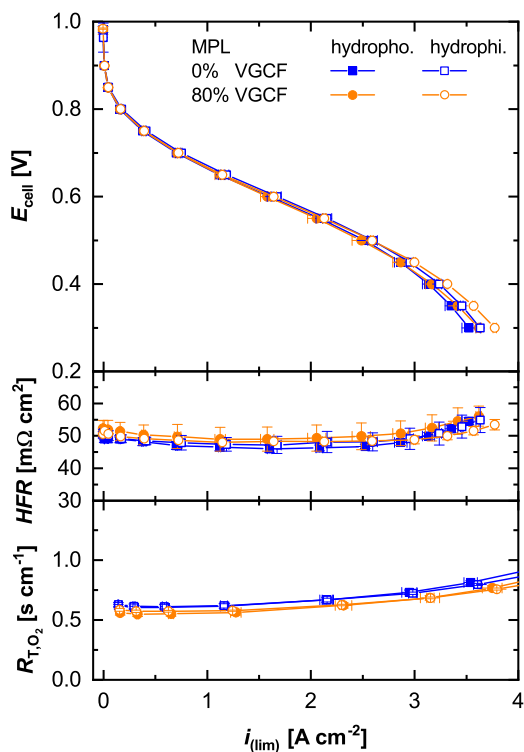


Figure 12. Differential-flow H_2/air polarization curves under **dry conditions** ($T_{\text{cell}} = 80^\circ\text{C}$, $RH = 70\%$, $p_{\text{abs}} = 170$ kPa) showing cell voltage (E_{cell} , top) and high frequency resistance (HFR , middle) versus current density (i) as well as total oxygen transport resistance (R_{T,O_2} , bottom) versus the limiting current density (i_{lim}) for the following cathode MPLs coated on the Freudenberg GDL-substrate: 0% VGCF with hydrophobic PTFE (blue line, full squares) or hydrophilic PFSA (blue line, empty squares) as binder, and 80% VGCF with PTFE (orange line, full squares) or PFSA (orange line, empty squares) as binder. The limiting current density is measured for various dry oxygen contents ($x_{\text{O}_2,\text{dry}}$) between 0.5% and 28%. The error bars represent the standard deviation of two independently measured cells. Data of the hydrophobic 0% VGCF MPL is taken from Reference 15.

an indication that the different binders and preparation procedures do not significantly affect the effective diffusivity in the dry MPL, and hence, porosity and tortuosity are expected to be independent of the binder.

At higher current densities of >0.5 A cm^{-2} , water starts to condense in the porous media and R_{T,O_2} increases significantly until it reaches a higher level at $i_{\text{lim}} > 1.5$ A cm^{-2} , with all hydrophilic MPLs (open symbols) exhibiting significantly higher R_{T,O_2} values compared to their hydrophobic counterparts, whereby the 80% VGCF MPLs have lower values than the 0% VGCF MPLs. Additionally, in the region with substantial liquid water content in the porous media (i.e., at >1.5 A cm^{-2}), the hydrophobic MPLs (full symbols) reveal only a slightly positive slope of R_{T,O_2} with increasing i_{lim} , while the hydrophilic MPLs (open symbols) show a significantly higher slope, indicating a continuous increase of water content in the porous media with increasing i_{lim} .

In the following we compare differential-flow H_2/air polarization curves and the associated high frequency resistances and oxygen transport resistances at dry conditions ($T_{\text{cell}} = 80^\circ\text{C}$, $RH = 70\%$, $p_{\text{abs}} = 170$ kPa, Figure 12) and humid conditions ($T_{\text{cell}} = 50^\circ\text{C}$, $RH = 120\%$, $p_{\text{abs}} = 300$ kPa, Figure 13) in order to evaluate the binder impact in the absence and presence of liquid water. At dry conditions (Figure 12), all materials perform similarly and reach a performance of around 1.6 A cm^{-2} at 0.6 V (top graph). Also, the HFR values (middle graph) and the R_{T,O_2} values of the hydrophilic MPLs are essentially identical with those of their hydrophobic counterparts. This indicates that the

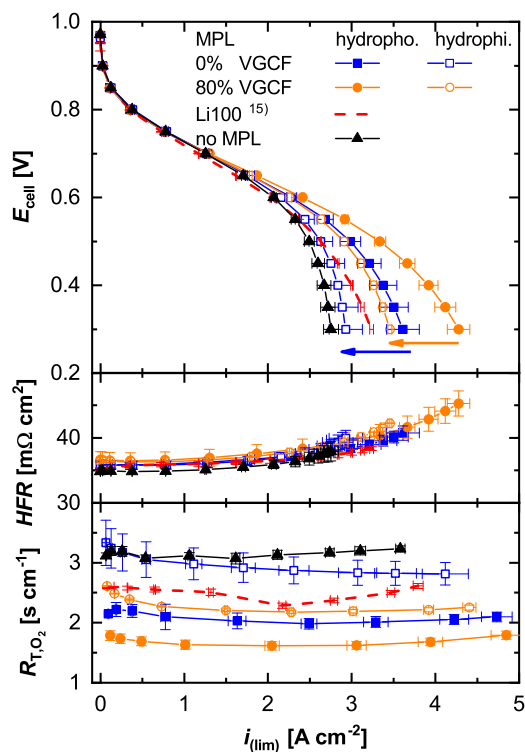


Figure 13. Differential-flow H_2/air polarization curves under **humid conditions** ($T_{\text{cell}} = 50^\circ\text{C}$, $RH = 120\%$, $p_{\text{abs}} = 300$ kPa) showing cell voltage (E_{cell} , top) and high frequency resistance (HFR , middle) versus current density (i) as well as total oxygen transport resistance (R_{T,O_2} , bottom) versus the limiting current density (i_{lim}) for the following for the Freudenberg GDL-substrate with no MPL (black) and the following cathode MPLs coated on the Freudenberg GDL-substrate: 0% VGCF with hydrophobic PTFE (blue line, full squares) or hydrophilic PFSA (blue line, empty squares) as binder, 80% VGCF with PTFE (orange line, full squares) or PFSA (orange line, empty squares) as binder, and Li100 MPL with PTFE as binder (red dotted line; data taken from Reference 15). The limiting current density is measured for various dry oxygen contents ($x_{\text{O}_2,\text{dry}}$) between 0.5% and 28%. The error bars represent the standard deviation of two independently measured cells. Data of the hydrophobic 0% VGCF MPL, no MPL and the Li100 MPL are taken from Reference 15.

binder type does not affect the humidification of the membrane, the HFR , the binder volume fraction (at this low relative humidity), and the binder distribution.

On the other hand, the differential-flow H_2/air performance curves at humid conditions differ significantly from each other (Figure 13, top), as one would have expected based on the high i_{lim} -region shown in Figure 11. For both hydrophobic and hydrophilic binder, the 80% VGCF MPLs (orange lines/symbols) perform better than the 0% VGCF MPLs (blue lines/symbols), whereby the hydrophilic versions of these MPLs (open symbols) in both cases yield a ≈ 150 mA cm^{-2} lower performance at 0.6 V. This difference is even more pronounced at lower voltages, where the clear trend is highlighted by the blue and orange arrows in the upper panel of Figure 13. At the same time, however, the HFR values are essentially identical for all MPLs, independent of fiber content and binder type, so that the performance difference must be related to the oxygen transport resistance. This is indeed the case, and the R_{T,O_2} values for a given carbon composition of the MPL are always significantly higher for the hydrophilic MPLs. The observation that the hydrophilic 80% VGCF MPL (open orange symbols) shows a higher oxygen transport resistance than the hydrophobic 0% VGCF MPL (blue full symbols), which is the opposite of what we observe under the slightly higher-pressure conditions in Figure 11 (with $T_{\text{cell}} = 50^\circ\text{C}$, $RH = 77\%$, $p_{\text{abs}} = 400$ kPa) is likely due to the fact that in Figure 13 the inlet gas stream is already fully humidified at 120% RH , which means that a stable saturation of the

GDL-S/MPL with liquid water can already be achieved at lower current densities, while for $RH = 77\%$ (Figure 11), the saturation is still changing with current density, as indicated by the continuously increasing R_{T,O_2} with increasing limiting current density in the region of high water saturation in the porous media. As a reference, we included the GDL-substrate without MPL in Figure 13, showing the lowest performance and highest oxygen transport resistance, which is consistent with Tanuma et al., who has shown a similar result at humid operating conditions.²³

Discussion

Impact of MPL pore size on oxygen and water transport.—Even though, all tested hydrophobic MPLs, show very different properties, either in pore size distribution or in hydrophilicity, the materials perform similarly at dry conditions ($T_{cell} = 80^\circ\text{C}$, $RH = 70\%$, $p_{abs} = 170\text{ kPa}$), while differences are only observed at humid conditions ($T_{cell} = 50^\circ\text{C}$, $RH = 120\%$, $p_{abs} = 300\text{ kPa}$) and high pressure operation ($T_{cell} = 80^\circ\text{C}$, $RH = 100\%$, $p_{abs} = 300\text{ kPa}$). In this section, we will discuss the results and will seek to explain why the materials show this specific behavior.

From the SEM images of the prepared GDL-S/MPL materials (Figure 2) as well as from the mercury porosimetry data of either free-standing MPLs (Figure 3) or of MPLs on the final diffusion media (Figure 5), it becomes clear that by mixing different ratios of carbon black and VGCF, we can tune the porosity (ϵ), the pore size distribution, and the pore shapes of the MPL. Increasing the VGCF content leads to higher porosity and larger pore sizes, which in turn effectively impacts the ratio of tortuosity over porosity (τ/ϵ) and hence, the effective diffusivity.¹⁵ This means that with higher porosity, the effective diffusivity is increasing and the oxygen transport resistance is decreasing, as is observed in Figure 6 at small limiting current densities of $i_{lim} < 0.5\text{ A cm}^{-2}$. However, the impact of these small changes in R_{T,O_2} are very minor, because the MPL contributes to only a small fraction to the overall R_{T,O_2} . At dry conditions (Figure 7), R_{T,O_2} can be reduced by only $\approx 15\%$ between the 0% VGCF MPL and the best performing 100% VGCF, but the observed as well as the projected differences in H_2 /air performance at a relevant voltage of 0.6 V are negligible and within the error of measurement.

A significant impact of the cathode MPL composition on H_2 /air performance becomes visible in the presence of distinct amounts of liquid water in the porous media, which occur at our humid operating conditions ($T_{cell} = 50^\circ\text{C}$, $RH = 120\%$, $p_{abs} = 300\text{ kPa}$; see Figure 8) that are meant to mimick the transport conditions that occur during the warm-up process of a fuel cell stack. Here, even at 0.6 V, a clear trend of increasing current density and decreasing oxygen transport resistance with higher VGCF content and thus higher porosity and larger pore sizes becomes visible. This confirms that liquid water transport takes place more efficiently through larger pores, as has been shown previously for MPLs with large cracks or perforations.^{9,15,33,34,60–64} Previous studies already discussed the enhancing effect of adding small amounts of carbon nanotubes or aluminosilicate fibers, but mainly justified it with the hydrophilic properties of the fiber surface which would facilitate faster water absorption.^{28,29,31,36,65} On the other hand, our study strongly suggests that the improved performance of fiber containing MPLs is simply due to their larger porosity and their larger pore sizes, rather than the supposedly higher hydrophilicity of carbon fibers, since in all of our MPLs the relatively large PTFE binder content (20 wt%) renders the MPL very hydrophobic for MPLs both without and with carbon fibers. Nevertheless, as the possibility that hydrophilic domains are present in our MPLs cannot be excluded, we also examined the performance of carbon fiber based MPLs with hydrophobic (PTFE) and with hydrophilic binder (PFA), since this allows to clearly determine the effect of hydrophobic vs. hydrophilic properties for morphologically identical samples (see Figure 2).

The conceptual differences in transport properties of MPLs with differently sized pores and different hydrophobic/hydrophilic properties are illustrated in Figure 14, whereby the sketched small pore represents the small pores in carbon black based MPLs (see blue line

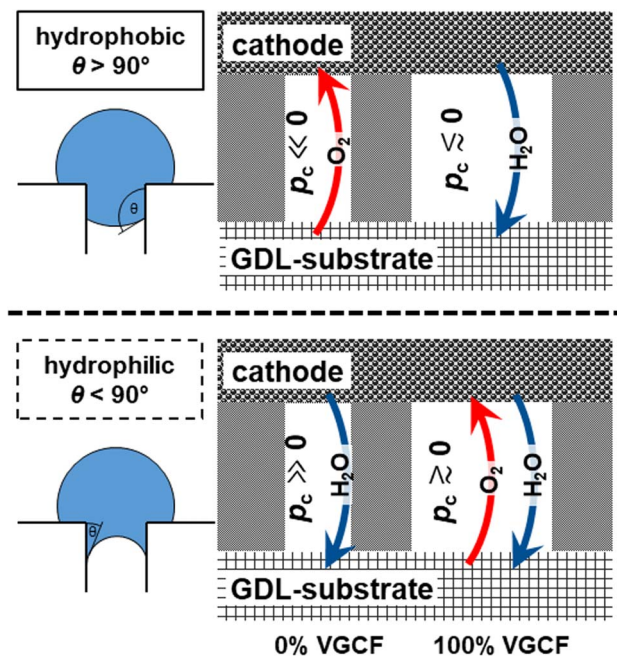


Figure 14. Illustration of capillary pressure p_c and the correspondent liquid water transport through MPL pores with different water contact angles ($\theta > 90^\circ \equiv$ hydrophobic; $\theta < 90^\circ \equiv$ hydrophilic) and with different pore sizes, whereby the large pores are most prevalent for VGCF based MPLs, and small pores are most prevalent in carbon black based MPLs.

in Figure 3 as well as purple and blue lines in Figure 5) and the sketched large pore represents the additional much larger pore sizes observed in the VGCF fiber containing MPLs (see Figure 3). According to the Young-Laplace equation (Eq. 1), a large hydrophobic pore (contact angle $\theta > 90^\circ$) has a smaller capillary pressure p_c than a small hydrophobic pore (negative sign), which means that for the latter a larger liquid pressure is necessary in order to wet the pore and transport water through it, particularly through small pores. As water is produced in the cathode catalyst layer and transported through the MPL toward the GDL-substrate, it will take the least resistive pathway through the largest pores. Small hydrophobic pores would be free of water and available for the opposing O_2 diffusion. For a wide pore size distribution between large and small pores, clearly observed for the VGCF containing MPLs with hydrophobic binder (see Figure 3), this bifunctional transport mechanism seems to effectively reduce the total oxygen transport resistance. This bifunctional transport mechanism is less effective for a narrow pore size distribution with mostly small hydrophobic pores found for the 0% VGCF MPL with hydrophobic binder (see Figure 3, particularly considering logarithmic scaling), where liquid water transport will take place through a larger pore volume fraction leading to more liquid water being retained at the MPL/cathode interface due to the higher capillary pressure. The commercial MPL with hydrophobic binder has even smaller pores and a very narrow pore size distribution with small pores (see Figure 5), which has the effect to even further increase R_{T,O_2} compared to the other hydrophobic MPLs.

At normal conditions (Figure 9 and Figure 10), no or minor amounts of liquid water are expected to be present in the porous media.¹⁵ This means that the performance is mainly limited by the dry transport through the porous MPL structure. As already indicated at dry conditions (Figure 7), the dry transport resistance decreases with increasing VGCF content. As the pressure dependent component of the oxygen transport resistance is proportional to the absolute gas pressure,^{43,44} a higher pressure increases the differences between different materials, as can be seen by comparing the R_{T,O_2} values at the low limiting current densities between Figure 6 (400 kPa_{abs}) and Figure 7 (170 kPa_{abs}). This has the effect, that the differential-flow fuel

cell performance at $T_{\text{cell}} = 80^{\circ}\text{C}$, $RH = 100\%$, $p_{\text{abs}} = 300$ kPa, the current density at 0.6 V increases by $\approx 40\%$ between the commercial and the 0% VGCF MPL and by $\approx 50\%$ between the commercial and the 100% VGCF MPL, both for 10% O_2/N_2 (Figure 9; mimicking stack outlet conditions) and for air (Figure 10; mimicking stack inlet conditions). Hence, the hydrophobic 100% VGCF MPL with its very broad pore size distribution containing large pores and with its high porosity performs best at low humidity, as it allows a facile bifunctional transport mechanism of liquid water through the larger pores and of oxygen through the smaller pores which remain free of liquid water due to their high capillary pressure. This is illustrated in the upper panel of Figure 14.

Impact of MPL hydrophilicity and hydrophobicity.—In the previous section we provided a rationale as to why the larger pores produced by the addition of carbon fibers can improve the oxygen diffusivity in MPL with a hydrophobic binder, particularly under humid and normal operating conditions. In the following, we will focus on the binder properties and want to clarify, why in the literature all-hydrophilic MPLs are often presented as superior over conventional hydrophobic MPLs.^{19–22,35,66}

At dry conditions (Figure 12) and under conditions where no liquid water is present in the porous media (Figure 11 at small i_{lim}), the total oxygen transport resistance is similar for the MPLs with hydrophilic and hydrophobic binder when comparing MPLs with the same carbon composition, i.e., with the same morphology (0% VGCF or 80% VGCF). Consequently, at dry conditions the H_2/air performance is essentially identical for hydrophilic and hydrophobic MPLs (Figure 12), as is the *HFR*. In the absence of liquid water, the transport properties of the MPL are defined by its porosity and tortuosity and, as shown in Figure 12 do not depend on the hydrophobic/hydrophilic properties of the applied binder. This observation is rather conclusive, as the content of either the PFSA or the PTFE binder was identical (20 wt%) and as their densities are similar (≈ 2.1 g cm^{-3} and ≈ 2.2 g cm^{-3} , respectively), which means that the dry volume fractions of both binders in the MPLs are essentially identical. Considering an expected 10% weight gain due to the water uptake of the PFSA ionomer at $RH = 70\%$,⁵⁶ the wet volume fraction of the PFSA binder is expected to be only $\approx 15\%$ higher than that of PTFE (no volume change in contact with water), which is rather negligible considering that the estimated void volume fraction in the MPLs ranges between ≈ 68 – 83% for all the here tested MPLs.

In the presence of liquid water (Figure 11 at high i_{lim} and Figure 13) differences between the hydrophobic and the hydrophilic MPLs become visible. A hydrophilic pore has per definition a water contact angle of $< 90^{\circ}$ as illustrated in Figure 14 (lower panel), which results in a positive capillary pressure and a voluntary water-filling of the pores (the concave shape of the intruding water droplet is illustrated on the left). While small hydrophilic pores (as e.g., in the 0% VGCF MPL with PFSA binder) result in high (positive) capillary pressures, larger pores exhibit capillary pressures closer to ≈ 0 kPa. In the latter case, a pore can be relieved from water by a small additional pressure. The voluntary filling of hydrophilic pores results in a continuous blocking of these pores for oxygen transport, which is contrary to what is expected for hydrophobic pores, for which eruptive water transport mechanisms are proposed, due to which the extent of the liquid water content in a given pore is changing periodically over time.^{34,62,67,68} As these phenomena strongly depend on the pore size distribution, the transport properties of hydrophilic vs. hydrophobic pores must be compared for the same carbon composition, i.e., for the same morphology, porosity, and pore size distribution (hydrophilic/hydrophobic 0% VGCF MPL or hydrophilic/hydrophobic 80% VGCF MPL). Doing so, it becomes obvious that the oxygen transport resistances are always lower for hydrophobic compared to hydrophilic MPLs, consistent with the superior H_2/air performance at high current densities (see Figure 11 and Figure 13). As one would expect from our earlier discussion, the 80% VGCF MPLs are always performing better than the 0% VGCF MPL because of its larger pores, as their absolute capil-

lary pressure is smaller, which facilitates water removal from/through large pores.

In summary, as the hydrophilic binder in both cases increases R_{T,O_2} and lowers the fuel cell performance at humid operating conditions, while at the same time no advantages are observed at dry operating conditions, we can conclude unequivocally that all-hydrophilic MPLs are not advantageous for fuel cell operation. Furthermore, we expect severe issues at sub-zero temperatures. Although Tabe et al. reported an improved freeze-start up when using a hydrophilic carbon fiber MPL instead of a hydrophobic carbon black as the hydrophobic MPL, which formed an ice layer at the interface to the cathode catalyst layer, we do believe that this behavior rather arises from the higher ice capacity due to the higher pore volume of the carbon fiber MPL than from the hydrophilic binder.⁶⁹ In particular due to the fact that hydrophilic pores are not easy to dry out during the shut-down process, significant issues are expected at sub-zero temperatures, at which residual water freezes and due to volume expansion may break the MPL and possibly the adjacent electrode.⁷⁰

This still leaves the question as to why other authors found significant fuel cell performance enhancements of all-hydrophilic MPLs compared to hydrophobic MPLs.^{21–30,36,37} Inspecting the MPL compositions used in these studies, it becomes apparent that the effect of different binders was compared for MPLs with a different composition of carbon materials. In References 21–24,30,35,66 for example, Aoyama et al. and Tanuma et al. compare hydrophobic carbon black based MPLs with hydrophilic carbon fiber based MPLs, which according to Figure 3 will have totally different pore size distribution, therefore varying simultaneously both pore sizes and hydrophilicity/hydrophobicity; while these authors show that the pore size distributions of their hydrophilic and hydrophobic MPL are very different (by SEM images or PSD measurements), they do not explicitly consider this effect in their analysis.^{19–24,30,35,66} In their latest publication,³⁰ however, Aoyama et al. reported MPL compositions with either carbon black (CB) or the same carbon fibers (CF) as were used in our study, both with either hydrophobic PTFE or hydrophilic PFSA as binder. Their obtained differential-flow H_2/air performance at high current densities (taken at 70°C , 100% RH, $p_{\text{out}} = 101$ kPa_{abs} (information kindly provided by the authors); MEA properties are unspecified) is essentially identical for all their 15 μm thick MPLs, i.e., for a hydrophobic CB MPL, a hydrophilic CB MPL, and a hydrophilic CF MPL (1.43 ± 0.01 A cm^{-2} at 0.4 V and 1.81 ± 0.02 A cm^{-2} at 0.2 V). This seems to be in contrast with our results, where under wet operating conditions hydrophilic MPLs with the same carbon material perform clearly worse than hydrophobic MPLs, and where CB based MPLs with the same binder perform clearly worse than CF based MPLs. One explanation might be that their testing conditions more closely reflect our “dry” conditions (80°C , 70% RH, 170 kPa; see Figure 7) where differences between the carbon material do not become apparent compared to our “humid” conditions (see Figure 8). This is indicated by the fact that when conducting our fuel cell measurements at 80°C , 100% RH, and 170 kPa (only change is from RH of 70% to a fully saturated gas stream; graph not shown in this paper), we also did not see any difference between hydrophilic and hydrophobic MPLs as in Figure 7. This unexpected phenomenon has been already discussed in our previous study (compare Figures 7a and 7b in Reference 15) and was explained by the absence of liquid water in the GDL-substrate (presumably by a high temperature gradient within the GDL-substrate) even at 100% RH. As Aoyama et al. also uses a Freudenberg GDL-substrate (with presumably a similar thermal conductivity as ours) and the operating pressure is lower than in our study (101 kPa_{abs} vs. 170 kPa_{abs}) suggesting a higher water uptake of the gas streams, we believe that the liquid water content at their operating conditions is comparably low and that their results are mainly dominated by the dry oxygen transport.

When considering an MPL thickness of 40 μm , the H_2/air performance of the hydrophobic CF MPL is the same as for the 15 μm variants (i.e., as above), while thicker hydrophilic CF MPL was clearly superior (≈ 1.78 A cm^{-2} at 0.4 V and ≈ 2.15 A cm^{-2} at 0.2 V). In our view, it is somewhat perplexing that the 40 μm thick hydrophilic CF

MPL would perform better than the 15 μm thick CF MPL, an effect which the authors hypothesize to be due to the higher surface area for water evaporation which is provided within the thicker hydrophilic CF MPL. While the thickness of the MPLs examined in our study ($30 \pm 5 \mu\text{m}$) is closer to the thicker MPLs examined by Aoyama et al.,³⁰ in contrast to their findings we clearly see a superior H_2/air performance and a lower oxygen transport resistance at humid conditions for all hydrophobic MPLs compared to the hydrophilic MPLs of the same carbon composition (see Figure 11 and Figure 13). The origin of this discrepancy is not clear. It may be due to the fact that MPLs do have optima in thickness (trade-off between transport properties and resistances)^{8,71,72} or in the binder/carbon ratio (a higher PFSA content of 41% has shown better performance at 80°C and 100% RH),²³ and that perhaps these optima are different for hydrophobic and hydrophilic MPLs.

In summary, the data shown in the present study with MPLs of equal thickness show a different trend with regards to the effect of hydrophilic vs. hydrophobic binders in the MPL: (i) When comparing samples with the same thickness and the same carbon materials and hence, structure (see Figure 2 and Figure 4), we can conclude unequivocally that hydrophobic MPLs always perform superior compared to hydrophilic MPLs, which is consistent with established water transport mechanisms. (ii) However, considering the strong effect of pore size distribution on MPL performance, one should of course be able to find a hydrophobic MPL which performs superior over a hydrophilic MPL based on a different carbon material which yield a more advantageous pore size distribution. To illustrate this possibility, we also investigated the fuel cell performance and the oxygen transport properties of a hydrophobic MPL based on a carbon black which we had examined in a previous study (Li100 carbon black from Denka), which is shown in Figure 13 (red symbols/lines; data taken from our previous publication¹⁵). This hydrophobic Li100 carbon black based MPL clearly performs worse than the hydrophilic 80% VGCF MPL, but this is not due to the hydrophobic binder in the former, but due to its unfavorable pore size distribution with a PSD-maximum at $\approx 70 \text{ nm}$ (see Figure 4 in Reference 15) compared to the 80% VGCF MPL of $\approx 490 \text{ nm}$ (see Figure 3).

Hence, we cannot find any scientifically rigorous proof for the claimed superiority of all-hydrophilic MPLs with regards to oxygen transport and fuel cell performance. As a matter of fact, our data and analysis suggest the opposite, namely that hydrophobic MPLs are superior to hydrophilic MPLs under fuel cell operating conditions where liquid water transport is required. This, however, does not mean, that hydrophilic regions in the MPL are unfavorable per se. MPLs with both hydrophilic and hydrophobic sites are supposed to be advantageous for parallel liquid water and oxygen transport as already shown for diffusion media which are designed such that they provide regions of μm -sized domains with distinctly hydrophilic and distinctly hydrophobic properties in the MPL.^{73,74} However, sophisticated preparation methods are necessary to effectively create these different domains within an MPL and their economic viability is currently unclear.

Conclusions

The present study investigates the influence of the pore size distribution of MPLs with hydrophobic PTFE or hydrophilic PFSA ionomer binder on fuel cell performance and on the oxygen transport resistance. We prepared hydrophobic MPLs with different compositions of acetylene black and vapor grown carbon fibers (VGCF; VGCF content of 0%, 50%, 80% and 100%) and found by mercury porosimetry that the porosity and the pore size distribution maximum of the MPLs increases with the VGCF content. SEM images visually confirm the more porous and more open structure of the VGCF containing MPLs compared to the acetylene black based MPL.

At fuel cell operation in the absence of liquid water ($T_{\text{cell}} = 80^\circ\text{C}$, $p_{\text{abs}} = 170 \text{ kPa}$, $RH = 70\%$), all materials perform similarly. However, explicit differences are detected at relevant automotive operating condition ($T_{\text{cell}} = 80^\circ\text{C}$, $p_{\text{abs}} = 300 \text{ kPa}$, $RH = 100\%$) with the 100% VGCF MPL with hydrophobic binder performing $\approx 48\%$ better at 0.6 V better

than the commercial reference MPL, which can be attributed to the larger porosity and the very wide pore size distribution with a significant fraction of large pores of the 100% VGCF MPL. In the presence of significant amounts of liquid water, a clear trend is observed that larger pore sizes enhance fuel cell performance and reduce the oxygen transport resistance. We propose that this is due to a bifunctional transport mechanism, improving the parallel transport of oxygen to the electrode in small pores and of liquid water to the GDL-substrate in large pores. We rationalize this observation with the lower capillary pressure of larger hydrophobic pores decreasing the backpressure at the MPL/cathode interface, which is necessary in order to transport water through the MPL.

By replacing PTFE with PFSA ionomer binder, we prepared hydrophilic MPLs based on 0% VGCF and 80% VGCF content with hydrophilic pores, which are structurally indistinguishable from their hydrophobic counterparts as shown by SEM images. While in the absence of liquid water no significant differences in fuel cell performance and oxygen transport are detected, at humid conditions with significant amounts of liquid water a decrease in performance and in increase of oxygen transport resistance for the hydrophilic MPLs is observed, rationalized by liquid water filling of hydrophilic pores. Despite numerous claims in the literature that hydrophilic MPLs may provide superior fuel cell performance and lower oxygen transport resistance, a scientifically rigorous comparison of hydrophobic and hydrophilic MPLs using the same carbon composition (i.e., the same pore size distribution and porosity), unequivocally proves that the investigated hydrophilic MPLs are not performing better under the considered dry operating conditions ($T_{\text{cell}} = 80^\circ\text{C}$, $p_{\text{abs}} = 170 \text{ kPa}$, $RH = 70\%$) and that the hydrophobic MPLs are always superior at the here considered humid conditions ($T_{\text{cell}} = 50^\circ\text{C}$, $p_{\text{abs}} = 300 \text{ kPa}$, $RH = 120\%$).

Acknowledgments

This research was carried out within the framework of the joint project "Optigaa2". Financial support by the German Federal Ministry of Economic Affairs and Energy (grant number 03ET6015E), Freudenberg Performance Materials SE & Co. KG and Daimler AG is gratefully acknowledged. We are very thankful for the valuable discussions with Achim Bock (Freudenberg). The authors would also like to thank Kerstin Fischinger (ZSW Ulm) for the mercury porosimetry measurements, Katia Rodewald (Wacker-Chair of Macromolecular Chemistry, TUM) for the SEM measurements and David Müller (Chair of Technical Electrochemistry, TUM) for the development of the MPL preparation procedure. Furthermore, we appreciate the free of charge support of materials from Freudenberg, Germany (GDL substrate and commercial MPL), Denka, Japan (Li400 acetylene black), and 3M Dyneon, Germany (TF 5035GZ PTFE dispersion).

List of Symbols

Variable	Unit	Description
A	cm^2	area
D_{eff}	$\text{m}^2 \text{ s}^{-1}$	effective diffusion coefficient
d_{MPL}	μm	MPL thickness
d_{particle}	μm	particle diameter
d_{pore}	μm	pore diameter
E_{cell}	V	cell voltage
HFR	$\Omega \text{ cm}^2$	high frequency resistance
i	A cm^{-2}	current density normalized to geometric electrode area
i_{lim}	A cm^{-2}	limiting current density normalized to geometric electrode area
m	g	mass
p_{abs}	kPa	absolute pressure
$p_{\text{H}_2\text{O}}$	kPa	partial pressure of water (at cell inlet)

Variable	Unit	Description	
R_{T,O_2}	$s\text{ cm}^{-1}$	total oxygen transport resistance	
R_{x,O_2}	$s\text{ cm}^{-1}$	oxygen transport resistance of the component x (GDL, MPL, flow field, electrode)	
RH	%	relative humidity	
T_{cell}	$^{\circ}\text{C}$	fuel cell temperature	
V	ml	volume	
w	wt%	mass fraction	
$x_{O_2,\text{dry}}$	%	dry mole fraction of oxygen	
Constant	Value	Unit	Description
F	96485	C mol^{-1}	Faraday constant
R	8.3145	$\text{J mol}^{-1}\text{ K}^{-1}$	ideal gas constant
Greek letter	Unit	Description	
γ_{H_2O}	N m^{-1}	surface tension of water	
γ_{Hg}	N m^{-1}	surface tension of mercury	
ε	%	porosity	
θ	$^{\circ}$	contact angle	
ρ	g cm^{-3}	density	
τ	-	tortuosity	

ORCID

Christoph Simon  <https://orcid.org/0000-0002-2381-7641>
 Hubert A. Gasteiger  <https://orcid.org/0000-0001-8199-8703>

References

- W. Gu, D. R. Baker, Y. Liu, and H. A. Gasteiger, in *Handbook of Fuel Cells*, Vol. 6, W. Vielstich, H. A. Gasteiger, and A. Lamm, Editors, p. 631, John Wiley & Sons, Ltd (2009).
- A. Weber, R. Darling, J. Meyers, and J. Newman, in *Handbook of Fuel Cells*, Vol. 1, W. Vielstich, H. A. Gasteiger, and A. Lamm, Editors, p. 47, John Wiley & Sons, Ltd (2010).
- J. P. Owejan, J. E. Owejan, W. B. Gu, T. A. Trabold, T. W. Tighe, and M. F. Mathias, *J. Electrochem. Soc.*, **157**, B1456 (2010).
- M. F. Mathias, J. Roth, J. Fleming, and W. Lehnert, in *Handbook of Fuel Cells*, Vol. 3, W. Vielstich, H. A. Gasteiger, and A. Lamm, Editors, p. 517, John Wiley & Sons, Ltd (2010).
- L. Cindrella, A. M. Kannan, J. F. Lin, K. Saminathan, Y. Ho, C. W. Lin, and J. Wertz, *J. Power Sources*, **194**, 146 (2009).
- J. M. Morgan and R. Datta, *J. Power Sources*, **251**, 269 (2014).
- S. Park, J.-W. Lee, and B. N. Popov, *Int. J. Hydrogen Energy*, **37**, 5850 (2012).
- P. Antonacci, S. Chevalier, J. Lee, N. Ge, J. Hinebaugh, R. Yip, Y. Tabuchi, T. Kotaka, and A. Bazylak, *Electrochim. Acta*, **188**, 888 (2016).
- J. T. Gostick, M. A. Ioannidis, M. W. Fowler, and M. D. Pritzker, *Electrochem. Commun.*, **11**, 576 (2009).
- Y. Tabe, Y. Aoyama, K. Kadowaki, K. Suzuki, and T. Chikahisa, *J. Power Sources*, **287**, 422 (2015).
- F. Lufrano, E. Passalacqua, G. Squadrito, A. Patti, and L. Giorgi, *J. Appl. Electrochem.*, **29**, 445 (1999).
- S. Park, J.-W. Lee, and B. N. Popov, *J. Power Sources*, **177**, 457 (2008).
- E. Passalacqua, G. Squadrito, F. Lufrano, A. Patti, and L. Giorgi, *J. Appl. Electrochem.*, **31**, 449 (2001).
- C. S. Kong, D.-Y. Kim, H.-K. Lee, Y.-G. Shul, and T.-H. Lee, *J. Power Sources*, **108**, 185 (2002).
- C. Simon, D. Kartouzian, D. Müller, F. Wilhelm, and H. A. Gasteiger, *J. Electrochem. Soc.*, **164**, F1697 (2017).
- L. R. Jordan, A. K. Shukla, T. Behrsing, N. R. Avery, B. C. Muddle, and M. Forsyth, *J. Appl. Electrochem.*, **30**, 641 (2000).
- X. L. Wang, H. M. Zhang, J. L. Zhang, H. F. Xu, Z. Q. Tian, J. Chen, H. X. Zhong, Y. M. Liang, and B. L. Yi, *Electrochim. Acta*, **51**, 4909 (2006).
- X. L. Wang, H. M. Zhang, J. L. Zhang, H. F. Xu, X. B. Zhu, J. Chen, and B. L. Yi, *J. Power Sources*, **162**, 474 (2006).
- T. Tanuma, M. Kawamoto, and S. Kinoshita, *J. Electrochem. Soc.*, **164**, F499 (2017).
- T. Tanuma and M. Kawamoto, *ECS Transactions*, **69**, 1323 (2015).
- Y. Aoyama, K. Suzuki, Y. Tabe, T. Chikahisa, and T. Tanuma, *ECS Transactions*, **64**, 527 (2014).
- Y. Aoyama, K. Suzuki, Y. Tabe, T. Chikahisa, and T. Tanuma, *ECS Transactions*, **69**, 743 (2015).
- T. Tanuma, *J. Electrochem. Soc.*, **157**, B1809 (2010).
- T. Tanuma and S. Kinoshita, *Energy Procedia*, **28**, 12 (2012).
- T. Kitahara, H. Nakajima, M. Inamoto, and M. Morishita, *J. Power Sources*, **234**, 129 (2013).
- T. Kitahara, H. Nakajima, and K. Mori, *J. Power Sources*, **199**, 29 (2012).
- T. Kitahara, H. Nakajima, and K. Okamura, *ECS Transactions*, **69**, 1313 (2015).
- T. Kitahara, H. Nakajima, and K. Okamura, *J. Power Sources*, **283**, 115 (2015).
- R. Schweiss, M. Steeb, and P. M. Wilde, *Fuel Cells*, **10**, 1176 (2010).
- Y. Aoyama, Y. Tabe, R. Nozaki, K. Suzuki, T. Chikahisa, and T. Tanuma, *J. Electrochem. Soc.*, **165**, F484 (2018).
- D. Spornjak, R. Mukundan, R. L. Borup, L. G. Connolly, B. I. Zackin, V. De Andrade, M. Wojcik, D. Y. Parkinson, D. L. Jacobson, D. S. Hussey, K. L. More, T. Chan, A. Z. Weber, and I. V. Zenyuk, *ACS Applied Energy Materials*, **1**, 6006 (2018).
- I. V. Zenyuk, E. C. Kumbur, and S. Litster, *J. Power Sources*, **241**, 379 (2013).
- Z. Lu, J. Waldecker, M. Tam, and M. Cimenti, *ECS Transactions*, **69**, 1341 (2015).
- H. Markotter, J. Haussmann, R. Alink, C. Totzke, T. Arlt, M. Klages, H. Rieseheimer, J. Scholta, D. Gerteisen, J. Banhart, and I. Manke, *Electrochem. Commun.*, **34**, 22 (2013).
- T. Tanuma and S. Kinoshita, *J. Electrochem. Soc.*, **159**, B150 (2012).
- T. Kitahara, H. Nakajima, and K. Okamura, *ECS Transactions*, **64**, 477 (2014).
- T. Kitahara and H. Nakajima, *Int. J. Hydrogen Energy*, **41**, 9547 (2016).
- J. Lee, R. Banerjee, M. G. George, D. Muirhead, P. Shrestha, H. Liu, N. Ge, S. Chevalier, and A. Bazylak, *J. Electrochem. Soc.*, **164**, F1149 (2017).
- P. Shrestha, R. Banerjee, J. Lee, N. Ge, D. Muirhead, H. Liu, A. K. C. Wong, D. Ouellette, B. Zhao, and A. Bazylak, *J. Power Sources*, **402**, 468 (2018).
- A. Z. Weber, R. M. Darling, and J. Newman, in *J. Electrochem. Soc.*, Vol. **151**, p. A1715 (2004).
- K. G. Gallagher, R. M. Darling, T. W. Patterson, and M. L. Perry, *J. Electrochem. Soc.*, **155**, B1225 (2008).
- D. R. Baker, C. Wieser, K. C. Neyerlin, and M. W. Murphy, *ECS Transactions*, **3**, 989 (2006).
- D. R. Baker, D. A. Caulk, K. C. Neyerlin, and M. W. Murphy, *J. Electrochem. Soc.*, **156**, B991 (2009).
- D. A. Caulk and D. R. Baker, *J. Electrochem. Soc.*, **157**, B1237 (2010).
- D. A. Caulk and D. R. Baker, *J. Electrochem. Soc.*, **158**, B384 (2011).
- J. P. Owejan, T. A. Trabold, and M. M. Mench, *Int. J. Heat Mass Transfer*, **71**, 585 (2014).
- C. Simon, F. Hasché, and H. A. Gasteiger, *J. Electrochem. Soc.*, **164**, F591 (2017).
- H. Oh, Y. I. Lee, G. Lee, K. Min, and J. S. Yi, *J. Power Sources*, **345**, 67 (2017).
- J. P. Owejan, J. E. Owejan, and W. B. Gu, *J. Electrochem. Soc.*, **160**, F824 (2013).
- T. A. Greszler, D. Caulk, and P. Sinha, *J. Electrochem. Soc.*, **159**, F831 (2012).
- C. Simon, F. Hasché, D. Müller, and H. A. Gasteiger, *ECS Transactions*, **69**, 1293 (2015).
- A. Orfanidi, P. J. Rheinländer, N. Schulte, and H. A. Gasteiger, *J. Electrochem. Soc.*, **165**, F1254 (2018).
- P. Zihur, I. Hartung, S. Kirsch, G. Huebner, F. Hasché, and H. A. Gasteiger, *J. Electrochem. Soc.*, **163**, F492 (2016).
- A. Kongkanand and M. F. Mathias, *The Journal of Physical Chemistry Letters*, **7**, 1127 (2016).
- C. S. Gittleman, F. D. Coms, and Y.-H. Lai, in *Polymer Electrolyte Fuel Cell Degradation*, Vol. 1, M. M. Mench, E. C. Kumbur, and T. N. Veziroglu, Editors, p. 15, Academic Press, Boston (2012).
- C. K. Mittelsteadt and H. Liu, in *Handbook of Fuel Cells*, Vol. 1, W. Vielstich, A. Lamm, and H. A. Gasteiger, Editors, John Wiley & Sons, Ltd (2010).
- S. Goswami, S. Klaus, and J. Benziger, *Langmuir*, **24**, 8627 (2008).
- S. De Almeida and Y. Kawano, *J. Therm. Anal. Calorim.*, **58**, 569 (1999).
- L. G. Lage, P. G. Delgado, and Y. Kawano, *J. Therm. Anal. Calorim.*, **75**, 521 (2004).
- R. Alink, J. Haussmann, H. Markotter, M. Schwager, I. Manke, and D. Gerteisen, *J. Power Sources*, **233**, 358 (2013).
- S. S. Alrwashdeh, H. Markötter, J. Haußmann, T. Arlt, M. Klages, J. Scholta, J. Banhart, and I. Manke, *Energy*, **102**, 161 (2016).
- P. Deevanhxay, T. Sasabe, S. Tsushima, and S. Hirai, *J. Power Sources*, **230**, 38 (2013).
- S. Prass, S. Hasanpour, P. K. Sow, A. B. Phillion, and W. Mérida, *J. Power Sources*, **319**, 82 (2016).
- T. Sasabe, P. Deevanhxay, S. Tsushima, and S. Hirai, *Electrochem. Commun.*, **13**, 638 (2011).
- R. Mukundan, J. Davey, J. D. Fairweather, D. Spornjak, J. S. Spendelow, D. S. Hussey, D. Jacobson, P. Wilde, R. Schweiss, and R. L. Borup, *ECS Transactions*, **33**, 1109 (2010).
- T. Tanuma and S. Kinoshita, *ECS Transactions*, **41**, 603 (2011).
- S. Litster, D. Sinton, and N. Djilali, *J. Power Sources*, **154**, 95 (2006).
- C. Hartnig, I. Manke, R. Kuhn, S. Kleinau, J. Goebbels, and J. Banhart, *J. Power Sources*, **188**, 468 (2009).
- F. Onishi, Y. Tabe, and T. Chikahisa, *ECS Transactions*, **86**, 89 (2018).
- S. Kim and M. M. Mench, *J. Power Sources*, **174**, 206 (2007).
- A. Z. Weber and J. Newman, *J. Electrochem. Soc.*, **152**, A677 (2005).
- S. Park, J.-W. Lee, and B. N. Popov, *J. Power Sources*, **163**, 357 (2006).
- A. Forner-Cuenca, J. Biesdorf, A. Lamibrac, V. Manzi-Orezzoli, F. N. Büchi, L. Gubler, T. J. Schmidt, and P. Boillat, *J. Electrochem. Soc.*, **163**, F1038 (2016).
- A. Forner-Cuenca, J. Biesdorf, V. Manzi-Orezzoli, L. Gubler, T. J. Schmidt, and P. Boillat, *J. Electrochem. Soc.*, **163**, F1389 (2016).